Precision Engineering 76 (2022) 208–225

Contents lists available at ScienceDirect

Precision Engineering

journal homepage: www.elsevier.com/locate/precision

A load cell with adjustable stiffness and zero offset tuning dedicated to electrical micro- and nanoprobing

M. Smreczak [*], L. Tissot-Daguette, E. Thalmann, C. Baur, S. Henein

Instant-Lab, École Polytechnique Fédérale de Lausanne (EPFL), Rue de la Maladière 71b, CH-2000, Neuchatel, Switzerland

ARTICLE INFO

Keywords:
Compliant mechanism
Load cell
Micromanipulation
Adjustable stiffness
Precise force sensing
Zero stiffness
Flexures

ABSTRACT

The tasks of electrical micro- and nanoprobing require precision that goes beyond human perception and therefore, depend on sensors providing real-time feedback. Efforts towards automation in micro- and nanoprobing and emerging areas such as branched nanowire networks, has resulted in a growing number of applications where electrical probing without simultaneous force control is insufficient. This article presents the design of a novel mesoscale flexure-based load cell dedicated to micro- and nanoprobing. By integrating systems for stiffness adjustment and a zero offset tuning, the force-displacement characteristic of the device can be adapted to suit a wide range of applications, from the measurement of large forces up to 60 mN to a resolution as high as 10.1 nN, and even negative stiffness (bistable) behavior. By controlling the tuning during measurements, a virtual dynamic range of $6.38 \cdot 10^6$ is achievable, which is one order of magnitude greater than existing commercial products. We validated the results experimentally on a titanium alloy prototype fabricated by electrical discharge machining (EDM). Experimental and finite element results were also used to validate the analytical model of the load-cell. Additionally, the device allows for probe tip replacement, which is a significant advantage compared to existing MEMS load cells, and comprises a gravity compensation system to accommodate a wide range of commercially available probe tips.

1. Introduction

1.1. Manipulation at the micrometric scale

The invention and development of microscopes focused attention of researchers and industry on micrometric-scale applications that are beyond human tactile perception. Subsequently, discoveries in the fields of microfabrication and microrobotics initiated the rapid development of micromanipulation in areas such as electrical microprobing, micro-assembly, biotechnology and others [1]. While the scale of manipulated objects has decreased and now often reaches sub-micrometer or even atomic scales, the term nanomanipulation has become popular [2].

Manipulating objects at a micrometric scale requires feedback to evaluate the interactions with them and to decide on the control. The most common feedback channels in micromanipulation are vision and force sensing, while electrical feedback is used for contact detection in a limited number of applications (e.g. Ref. [3]). Force feedback may complement the vision-based robot control as in Ref. [4], or it may be the only feedback channel when visual assessment is limited, e.g. due to the long image acquisition time, limited visual assessment of the interaction, or operating beyond the camera's field of view. Examples of tasks at the micro scale in which force feedback is beneficial are electrical probing [5], mechanical characterization [6], microgripping [7] and cell injection [8].

A micro- or nanomanipulator [9] is a device that uses external physical forces to manipulate objects at the micro- and nanoscale. It can serve as a universal positioning platform on which custom sensors and end effectors can be mounted. This article focuses on the design of a compact load cell suitable for integration with a micromanipulator, thus offering versatility in various micromanipulation tasks. An example schematic of such a system for electrical microprobing is shown in Fig. 1. The presented design also aims to be compatible with robotic manipulators since, compared to manual manipulators, they provide greater repeatability and allow for integration of advanced functions, e.g. to support positioning and interactions [10]. A major additional advantage of robotic manipulators is the potential for automation, which often requires force feedback to evaluate interactions with objects at micrometric scales.

---

[*] Corresponding author.
E-mail address: michal.smreczak@epfl.ch (M. Smreczak).

https://doi.org/10.1016/j.precisioneng.2022.03.009
Received 21 September 2021; Received in revised form 4 February 2022; Accepted 15 March 2022
Available online 31 March 2022
0141-6359/© 2022 Elsevier Inc. All rights reserved.

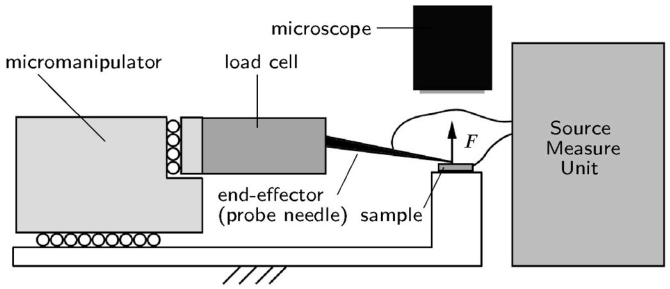

Fig. 1. Schematic of electrical microprobing with a single micromanipulator.

1.2. Micro- and nanoprobing applications requiring force feedback

The distinction between microprobing and nanoprobing is not well defined, but typically refers to the scale of the sample features being probed. However, many electrical probing applications take place at the intersection of these scales, and the majority of the methods and tools used are common to both microprobing and nanoprobing. For this reason, we will use the term micro- and nanoprobing in the rest of the article to emphasize the scope of the presented solutions, regardless of the scale.

This article focuses on the design of a load cell for electrical micro- and nanoprobing applications. An example of such applications are electronics produced using the bottom-up method (for example by growth or chemical synthesis process [11]), such as nanowire-based circuits, see Fig. 2. These have been gaining popularity in recent years, as reflected by the rapidly growing number of publications on the topic [12]. However, practical solutions to characterize them are still lacking. For instance, there are currently no reliable or common methods for the in situ electrical characterization of three-dimensional multiple nanowire-based circuits, also known as branched nanowires [13,14]. Micromanipulators with force feedback offer a promising solution since they decrease the risk of damaging the probe and sample from a too large force or losing contact when the force is too small.

Another field where electrical micro- and nanoprobing with force feedback is beneficial are applications in which the pressure of the probe tip on the sample affects the measured electrical signal, as in the case of piezoelectric materials [15]. Žukauskaitė et al. [16] describe nanoprobing of piezoelectric thin films, in which they performed the electrical measurement with simultaneous control of the pressure force applied to the sample. However, the nanoindenter used cannot be easily integrated into typical electrical micro- and nanoprobing applications that require independent positioning of multiple robots, such as in Ref. [17]. Alternatively, an atomic force microscope (AFM) probe was used for the nanoscale characterization of a piezoelectric polymer [18]. This probe allows the simultaneous high-accuracy measurement of current and force, but does not allow replacement of a probe tip or force sensitivity adjustment.

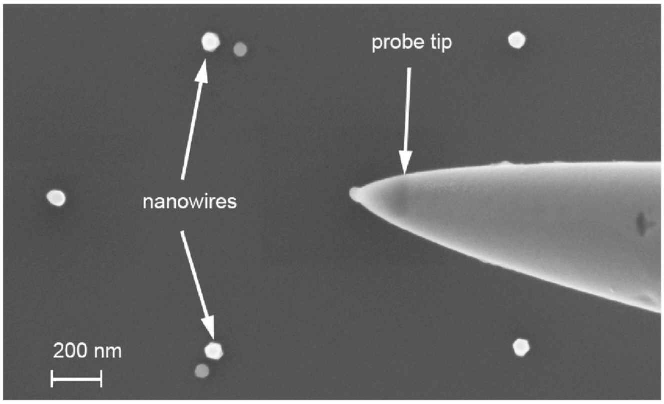

Fig. 2. Scanning Electron Microscope (SEM) image of in situ electrical characterization of vertical nanowires. The view from above makes it difficult to detect and assess the contact between the probe tip and the top of the nanowire. Force feedback is advantageous in such applications due to the limitations in visual assessment.

1.3. Challenges of force sensing in electrical micro- and nanoprobing

The issues listed below do not exhaust the list of challenges related to force measurement in all electrical micro- and nanoprobing applications, but solving them would be a significant contribution which constitutes the motivation for the research on the load cell presented in this article. Analysis of the various electrical microprobing applications listed in 1.2 and the challenges listed below form the a preliminary list of specifications for the load cell prototype; see Table 1.

1.3.1. Force measurement range

A large range of measurement is required since the variety of electrical micro- and nanoprobing applications results in a wide range of forces during probing. One of the major factors influencing their magnitude is the size of the sample and probe tip, ranging from a few nanometers to tens of micrometers. Another factor is the type of interaction (e.g. pressing, indenting, profiling) [10]. Additional factors are materials used, SEM chamber conditions and imaging parameters [19]. Although knowledge of electrical contact is well-established [20], practical force measurements in electrical micro- and nanoprobing are still poorly documented. Existing sources give a rough estimation of contact forces needed to establish an Ohmic contact ranging from about 10 μN up to 100 mN [21–23].

1.3.2. Variety of probe tips

The proposed sensor should provide a way of compensating for gravity effects caused by using various end effectors. Indeed, the probe needles used in micro- and nanoprobing may vary in shape, length, diameter, and material, which affects their mass and center of gravity. For example, the diameter of the tip depends on the scale of the sample, smaller for probing a chip produced by a 7 nm process than for probing features in the order of a few micrometers. The length of the probe needle often depends on the distance between the sample and the micromanipulator.

1.3.3. Probe tip replacement

It is important to be able to replace the end effector independently of the force-sensing part of the mechanism, see Fig. 3. Indeed, probe needles can be damaged or contaminated by contact with the sample. Additionally, their electrical properties may degrade due to oxidation. A major challenge is to achieve a high sensitivity of force measurement while having a sturdy device that will resist the forces occurring during

Table 1
Initial specifications used to design the load cell.

Parameter	Symbol	Value	Comment
Force resolution	R	$\leq 500\,nN$	Force sufficient to safely detect and maintain ohmic contact in electrical micro- and nanoprobing
Force range	F_{max}	±20 mN or more	Force sufficient to perform typical micromanipulation tasks
Load cell payload (i. e., probe mass)		between 70 mg and 310 mg	Measured on multiple different typical micro- and nanoprobing needles
Admissible force applied onto the lever in any direction		±2 N or more	Estimating the forces involved in careful manual probe tip replacement

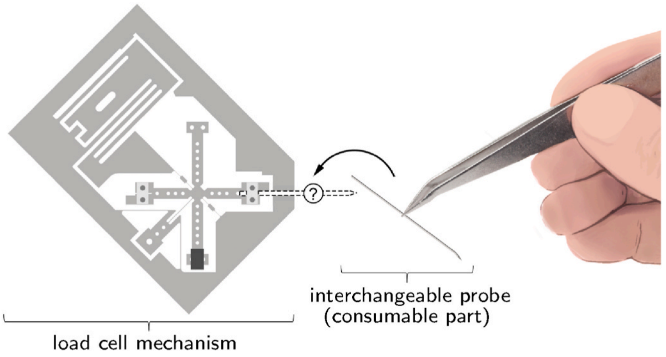

Fig. 3. The probe tip (end effector) is the consumable part of micro- and nanoprobing. For this reason, it is beneficial to use a force sensor that facilitates manual probe tip replacement.

replacement.

1.3.4. *Compatibility with various microscopes*

Features with a size larger than a micrometer can be observed under an optical microscope while, at the nanoscale, it is necessary to use another imaging method such as SEM. So, additional challenges arise for nanoprobing, such as operation in a vacuum and considerably limited space. It is therefore essential to design a compact load cell for which adjustments and readings can be carried out remotely, e.g. with the help of integrated actuators and remote sensor heads. A vacuum also imposes constraints on the mechanism, such as the absence of lubricants, which would evaporate.

1.3.5. *Force control*

Maintaining a stable electrical contact with the sample requires real-time force monitoring. In nanoprobing, visual feedback is often restricted during the measurement as the electron beam can interfere with the probe tip and sample. For this reason, it is important to minimize the response time of the load cell, and to provide a method for a continuous position refinement.

1.4. *Existing solutions*

1.4.1. *Force sensing at a micrometric scale*

A load cell (also referred to as a force sensor or a force transducer) acts as a transducer transforming the input force (pressure, load, tension, torque) into electric signal (digital or analog). The most common types of load cells dedicated to forces measured at micrometric scale are: strain gauge based, piezoresistive, capacitive, and optical [24]. If components of the sensor are made at the microscopic scale, they are classified as microelectromechanical systems (MEMS) [25].

The majority of solutions used in micromanipulation are flexure-based MEMS (e.g. Refs. [5,26,27]). Flexure mechanisms have the advantage of being compatible with microfabrication, producing high accuracy motions due to the absence of play and being compatible with vacuum environments due to the absence of friction and lubricant [28]. Additionally, the flexures used to guide the probe tip provide a stiffness that directly links the measured force to a displacement that can be conveniently measured. These are some of the advantages that have guided the choice of flexure mechanism for the device presented here. When these devices are implemented at the microscopic scale [5,26,27], they are characterized by low stiffness, which allows measurement of forces with high sensitivity. However, their small size results in high fragility which increases the risk of damaging the sensor during use. The small size of the sensor and the high level of integration make it impossible to replace parts of the mechanism, or to use commercial probe needles. As a result, an end-effector repair or replacement usually means replacing the entire mechanism. Although the optimization of microfabrication processes tends to decrease production costs [29], this factor remains a significant disadvantage of MEMS-based force sensors. We overcome this disadvantage in the presented device by aiming for a larger scale and providing a solution for probe tip replacement.

AFM-based solutions are one of the most often used solutions to measure force in micromanipulation. Simultaneous electrical probing and force sensing can be achieved with conductive AFM [30]. They achieve the sensitivity required for most microprobing applications, such as microassembly [31] and cell manipulation [8]. Their main disadvantage is the lack of possibility to adjust their stiffness after mounting a cantilever, which limits the range of applications where they can be used.

Self-sensing actuators (SSA) [32] constitute a relatively new group of solutions related to force sensing in micromanipulation. They enable force measurement and precise actuation to be performed by the same structure, hence their main advantage is the reduced size of the device. Recent studies on this technology, however, showed that modelling and processing the measurement signal is extremely challenging and sensitive to noise [33]. At this stage of development, the self-sensing piezoactuators do not provide sufficient precision for electrical micro- and nanoprobing.

Less popular solutions dedicated to small forces, such as magnetic, inductive, and commercial mesoscale load cells have been discussed in Ref. [34]. None of the existing technologies is currently used widely in electrical micro- and nanoprobing, probably because they do not fully address the challenges listed in 1.3.

1.4.2. *Gravity compensation*

As mentioned in Sec. 1.3, our sensor will use a variety of probe tips, which will affect its mass and center of gravity. As a result, gravity may significantly affect the sensor's reading and we must compensate for this.

Gravity compensated mechanisms have been known for thousands of years, and were already used in ancient Egypt [35]. Over the years, the development of gravity compensation mechanisms resulted in numerous inventions, for example the statically balanced Anglepoise lamp [36]. Nowadays, solutions using precise mechanisms of gravity compensation are widely used in such fields as metrology [37,38], robotics [39] and rehabilitation [40]. A review of passive gravity compensation methods is found in Ref. [41].

With miniaturization, gravity compensation using a counterweight becomes more challenging, however. Solutions exist that control the position of a sliding mass by means of a micro-metric screw [42]. This achieves a high level of precision but significantly increases the dimensions of the device. Alternatively, an electromagnet paired with a permanent magnet can be used to generate a force counteracting gravity [43].

Another group of gravity compensation mechanisms are those based on preloaded springs [44], sometimes used as bistable buckling beams [45]. On the one hand, the gravity compensation realized by the preloaded springs allows for a high adjustment accuracy, on the other hand, the spring-based compensation influences the dynamic properties of the mechanism.

Finally, active gravity compensation by force-controlled actuators is a solution often used in automatic control [46]. The advantages of active compensation are the possibility of close-loop control, real-time compensation of the variable weight and active vibrations damping. For example, this is used in MEMS accelerometers [47], where the electrostatic forces do the compensation.

1.4.3. *Force range and sensitivity adjustment*

As mentioned in Sec. 1.3, our sensor aims for a large force measurement range. This is typically associated with low force resolution, where force resolution is meant as the smallest detectable change in force measurement. One way to avoid this contradiction is to design a transducer with adjustable sensitivity, so that it can be adapted to the requirements of the application [24]. Such devices exist where the overall stiffness is adjusted with an electrostatic force [48] or by displacing a levitated magnet [49]. The latter is, however, sensitive to external magnetic fields and orientation with respect to gravity. Muntwyler et al. [27] proposed a 3-DoF MEMS force sensor with electronically tuned force range. The force sensing resolution is 30 nN and the tuning mechanism allows extending the force sensing range to 200 μN. As mentioned earlier, this MEMS solution does not allow for probe tip replacement or using commercial probe needles.

Alternatively, the force sensitivity of a flexure mechanism can also be tuned by changing its mass and the location of its center of gravity (CG). For instance, in Ref. [50], an analogous solution consisting of a kinematic chain with torsional springs at the joints achieved quasi zero-stiffness by compensating the spring forces with the weight of the links.

In our previous work [34], we described a flexure load cell whose stiffness we adjusted by controlling the preload of a spring. This resulted in a large sensitivity adjustment range for a relatively compact structure. Additionally, the tuning could be passive (e.g. using a screw), allowing to maintain a setting without an external source of energy, or active, enabling adjusting the sensitivity by means of an actuator. These advantages have led us to continue with this solution, except that we implement it at a smaller scale and take into account the effect of gravity.

Due to the limitations of typical force sensors, currently no commercially available universal compact solution exists that allows adjustment of the measurement precision and end effector replacement. Such a solution would be beneficial in applications with a large variety of samples (e.g. in electrical probing and biotechnology) and would allow better integration with universal micromanipulation platforms. This is hence the topic of this article.

1.5. Outline of the article

This article presents a new design and experimental verification of a load cell dedicated for electrical micro- and nanoprobing. In Sec. 2, we explain the general concepts behind the design of the load cell compliant mechanism. In Sec. 3, we develop the analytical model of the load cell in accordance with the three areas of focus of the design: stiffness adjustment, zero offset tuning and the impact of gravity on the load cell. In Sec. 4 we describe the dimensioning of the prototype, its finite element model and the probe tip replacement system. Then, we present the description and specification of the test bench used for characterization of the prototype in Sec. 5, followed by a discussion of the experimental results. Finally, we summarize the main contributions and future work in Sec. 6.

2. Design of the load cell

The design of the new compliant load cell is based on a lever whose pivoting motion with respect to the fixed frame is guided by flexures. As depicted in Fig. 4, when an input force F is applied to the tip of the probe, the lever deflects by an angle α, resulting in an output displacement x at the other extremity of the lever. By measuring the displacement x, the angle α can be found and, knowing the rotational stiffness of the pivot, the input force F can be estimated.

This load cell reuses some of the concepts from a previous load cell design [34], the main difference here being a simplified flexible structure called TIVOT [51] where the central pivot consists of three blades arranged in a T-shape. The flexure implementation of the mechanism is depicted in Fig. 5. The T-shaped pivot (1) consists of two longitudinal blades (1a) and a transversal blade (1b). The rigid lever (2) is used to amplify the input force applied to the probe tip (2a) and the output displacement of the reflector (2b). The motion of this reflector with respect to the fixed frame (6) is measured with a laser displacement sensor.

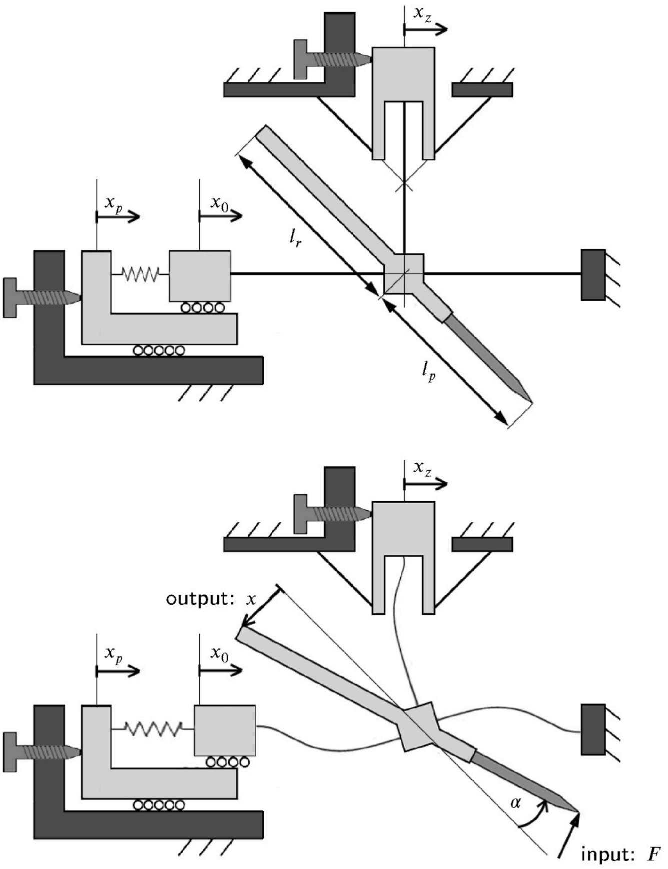

Fig. 4. Schematics of the new load cell, presenting the force to displacement transformation. The schematic on the top presents the mechanism at rest, whereas the schematic at the bottom presents the mechanism subjected to the input force *F*.

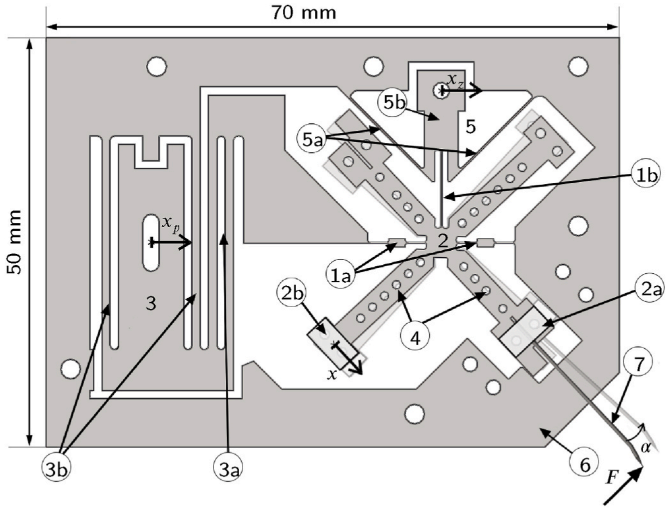

Fig. 5. Flexure implementation of the compliant load cell.

One of the main features of this load cell is the stiffness adjustment mechanism (3) consisting of a preloaded spring stage (3a) and a linear guide (3b), both realized with parallel flexures which are known to closely approximate a rectilinear motion [28]. This mechanism, described in detail in Sec. 3.1, allows decreasing the overall stiffness of the device to near-zero and beyond, turning the load cell into a bi-stable mechanism. This approach makes it possible to achieve a wide force measurement range while keeping high resolution when measuring small forces. Additionally, operating in bistable mode allows setting a threshold force that protects the sample and probe against damage. This feature has been improved compared to the previous design presented [52] by choosing dimensions for the transversal blade that enhance zero offset tuning and by reinforcing of longitudinal blades to increase the maximum preload force.

A major innovation of this design is the zero offset tuning (ZOT) mechanism (5) consisting of a remote center compliance (RCC [28]) joint (5a) and an adjustment lever (5b). This mechanism, described in detail in Sec. 3.3, grants adjusting the neutral position of the lever, i.e., to offset the force measurement range.

To facilitate the manual exchange of the probe tip (7), the prototype is designed in mesoscale, which also ensures high stiffness of the mechanism along its degrees-of-constraint (DoCs), i.e., directions other than the rotational DoF of the lever. Different weights of various probe tips can be compensated thanks to the CG-position adjustment mechanism (4) described in Sec. 4.3, as well as the ZOT mechanism.

The analytical model of the load cell allows freedom for dimensioning the mechanism, thus making it possible to achieve compatibility with a wide range of micro- and nanoprobing systems. The design of the load cell allows us to make it from vacuum-compatible and electrically conductive materials for use in electrical micro- and nanoprobing. The mechanism does not contain active electronic components and the displacement measurement is optical to minimize the temperature drift of the structure while probing. It is assumed that force measurements are done in real-time during probing so that it is possible to maintain a constant contact between the probe tip and the sample without requiring visual feedback from a microscope.

3. Analytical model

3.1. Stiffness adjustment mechanism

According to Euler-Bernoulli theory, the stiffness of elastic beams describes the relationship between a force and a torque acting on a beam and the resulting deflection. The stiffness of elastic joints can change with the increase in the elastic deformation, resulting in a non-linear restoring force as a function of the mechanism deflection. Therefore, to describe the relationship of the input force F to the output displacement x in the load cell, we define the overall tangent stiffness $k_t(x)$ given by

$$k_t(x) = \frac{\mathrm{d}F(x)}{\mathrm{d}x}. \tag{1}$$

The proposed load cell allows adjustment of the overall stiffness k_t. This is done by the adjustment of a preload spring stage depicted in Fig. 6 which generates a compression force P_0 acting on the longitudinal blades thus reducing their effective stiffness. The value of the compression force is controlled by the displacement x_p as follows

$$P_0 = k_p\left(x_p - x_0(\alpha)\right), \tag{2}$$

where x_0 is the sum of the shortenings of the two longitudinal blades when the pivot rotates by an angle α derived in [52, Eq. (13)], see Fig. 4.

Assuming the flexures of the preload stage are not subject to significant shear or torsion and the deformations are relatively small, we use equations from Ref. [28] based on Euler-Bernoulli beam theory to describe their stiffness

$$k_p = \frac{12EIn}{l^3}, \tag{3}$$

where

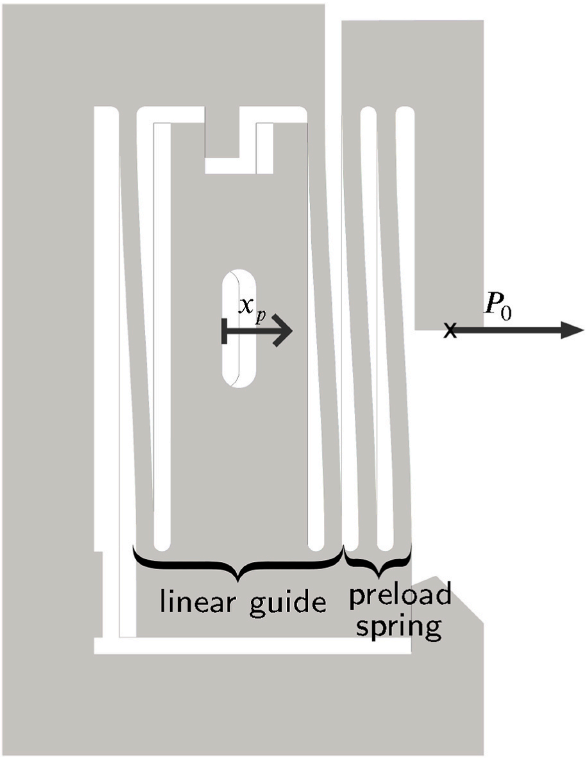

Fig. 6. Preload spring stage used for the stiffness adjustment of the load cell.

n is the number of parallel blades in the stage
l is the length of blades in the stage
I is second moment of area for a cross – section of a blade.

The admissible deflection of the preload stage is given by

$$x_{p\ max} = \frac{\sigma_{adm} l^2}{3Eh}, \tag{4}$$

where

σ_{adm} is the yield strength of the material divided by a safety factor
h is the width of a single blade.

The function of the linear guide is to ensure a rectilinear movement of the preload stage. The same length of guiding blades and preloaded blades cancels the parasitic lateral movement of the stage [28] during its pre-compression. The stiffness of the guide has no impact on the performance of the load cell, as the deformation of its blades is fixed by the external displacement adjustment.

A high compression force P_0 causes the longitudinal blades to have a negative stiffness, which can compensate or even surpass the positive stiffness of the transversal blade. As a result, it is possible to achieve an overall stiffness close to zero, referred to as near-zero stiffness, permitting the measurement of forces in the nano-newton range or a negative overall stiffness, turning the load cell into a bi-stable mechanism.

We derived the formula for the secant rotational stiffness of the preloaded TIVOT flexure in our previous work [52, Eq. (11)] and it has the form

$$k_{s,\alpha}\left(\alpha, x_p\right) = \frac{M\left(\alpha, x_p\right)}{\alpha} = 2k_{\alpha,lo}\left(\alpha, x_p\right) + k_{\alpha,tr}, \tag{5}$$

where $k_{\alpha,lo}$ is the secant rotational stiffness of a longitudinal blade subjected to a compression force P_0 given by Eq. (6) and $k_{\alpha,tr}$ is the rotational stiffness of the transversal blade given by Eq. (7).[1] Note that $k_{\alpha,tr}$ is constant.

$$k_{\alpha,lo} = \frac{EI_l}{\tilde{l}} A\tilde{l}\,\frac{A\tilde{l}\cos\left(A\tilde{l}\right) - \sin\left(A\tilde{l}\right)\left(1 + \left(A\tilde{l}\right)^2 \left(\frac{p}{\tilde{l}} + \left(A\tilde{l}\right)^2 \left(\frac{p}{\tilde{l}}\right)^2\right)\right)}{A\tilde{l}\sin\left(A\tilde{l}\right) + 2\left(\cos\left(A\tilde{l}\right) - 1\right)}, \tag{6}$$

where

$$A\left(\alpha, x_p\right) = \sqrt{\frac{P_0\left(\alpha, x_p\right)}{EI_l}}, \quad \text{see } P_0 \text{ in Eq.(2)}$$

$$E_l \text{ is Young's modulus of the used material}$$

$$I_l \text{ is the second moment of area for a cross-section of the longitudinal blade}$$

$$p \text{ is the distance between the axis of rotation and the closer end of the blade}$$

$$\tilde{l} \text{ is the length of a longitudinal blade.}$$

$$k_{\alpha,tr} = \frac{4EI_t\left(1 + \frac{3p}{\bar{l}} + 3\left(\frac{p}{\bar{l}}\right)^2\right)}{\bar{l}}, \tag{7}$$

where

$$I_t \text{ is the second moment of area for a cross-section of the transversal blade,}$$

$$\bar{l} \text{ is the length of the transversal blade.}$$

From Eq. (5), one can determine the force-displacement characteristic valid for small pivot angle $\alpha \cong \frac{x}{l_r}$

$$F_{flexure}\left(x, x_p\right) = \frac{k_{s,\alpha}\left(\frac{x}{l_r}, x_p\right)}{l_p l_r} x, \tag{8}$$

where l_p and l_r are depicted in Fig. 4.

Following Eq. (1), we then obtain the overall tangent stiffness $k_{t,flexure}(x, x_p)$ by differentiating Eq. (8). Since the probe tip deflection caused by interaction forces typically does not exceed several tens of micrometer in micro- and nanoprobing, the most significant quantity is the overall stiffness at the nominal position of the lever $k_{t,flexure}(x = 0, x_p)$. Around $x = 0$, $\alpha = 0$ and there is no beam shortening for both negative and positive stiffness ranges, i.e., $x_0(0) = 0$. As a result, $A(\alpha, x_p)$ becomes

$$A_0 = \sqrt{\frac{k_p x_p}{EI_l}}. \tag{9}$$

$k_t(x = 0, x_p)$ becomes

$$k_{t,flexure}\left(x = 0, x_p\right) = \frac{k_{\alpha,tr}}{l_p l_r} + 2\frac{EI_l}{l_p l_r} A_0 \frac{A_0\tilde{l}\cos\left(A_0\tilde{l}\right) - \sin\left(A_0\tilde{l}\right)\left(1 + A_0^2\tilde{l}p + A_0^2 p^2\right)}{A_0\tilde{l}\sin\left(A_0\tilde{l}\right) + 2\left(\cos\left(A_0\tilde{l}\right) - 1\right)} \tag{10}$$

We use equation (10) hereafter to design the prototype for different stiffness modes (positive, near-zero, negative), and given measurement ranges. The analytical model of the overall stiffness $k_t(x = 0, x_p)$ is also compared to finite element method (FEM) and the experimental results in Sec. 5.2.3. It is possible to do so, as gravity effects discussed in section 3.2 are negligible when using the prototype without additional ballast.

3.2. Impact of gravity on the load cell

Gravity may affect the measurement accuracy of the load cell. For this reason, this section provides a method for modelling and controlling the influence of gravity on the operation of the load cell.

To improve gravity insensitivity, the rigid lever of the TIVOT mechanism (without a probe tip) is balanced, which means that its CG is designed to coincide with its axis of rotation. However, the various probes used in micro- and nanoprobing attached to the lever influence the position of the CG. To analyze the effect of the CG offset from the axis of rotation of the lever, we break it down into two effects caused by the horizontal and vertical components of the offset, respectively perpendicular and parallel to the gravity vector. We do not analyze the out-of-plane offset of the CG as the FEM simulation proved that even a millimeter-scale offset in this direction does not have considerable effect on the operation of the mechanism.

An additional gravity effect is caused by the fact that the flexure pivots only approximate an ideal rotational motion, a property known as parasitic center shift [28,54]. As a result, the CG moves during the rotation of the lever, causing a change in the gravitational potential energy depending on the orientation of the load cell, which is known to influence the overall stiffness of the mechanism [37,53,55]. We model these three effects in detail below.

3.2.1. Effect of a horizontal CG offset on the load cell

The horizontal component of the CG distance from the rotation axis, labelled d_h in Fig. 7, produces a torque under the influence of gravity. The resulting reaction force sensed at the probe tip is

$$F_{gh} = gm_{lev}\frac{d_h}{l_p}\cos(\alpha) \overset{\alpha\approx 0}{\cong} gm_{lev}\frac{d_h}{l_p}, \tag{11}$$

where

$$g \text{ is the gravitational acceleration}$$

$$m_{lev} \text{is the mass of the lever with all ballast pins.}$$

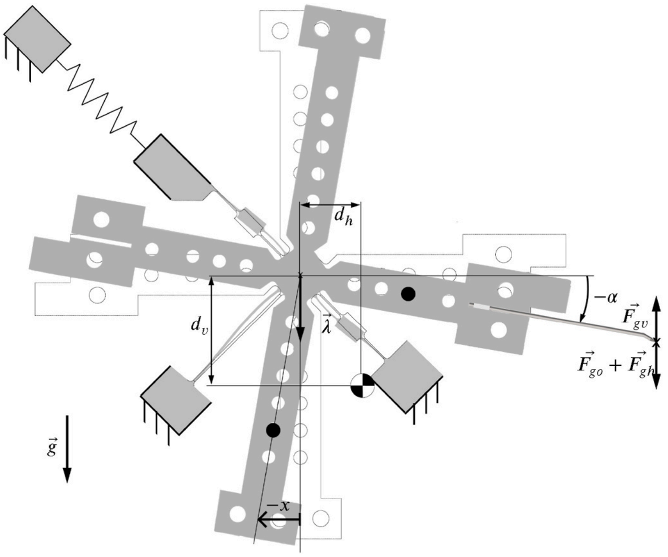

Fig. 7. Forces sensed at the tip of the probe resulting from the horizontal and vertical offset of the CG of the lever. Vector $\vec{\lambda}$ indicates the approximate direction of the parasitic shift of the T-shaped pivot rotational axis.

---

[1] For a rotational spring, the secant stiffness is defined as the restoring torque divided by the angular displacement $k_s = M(\alpha)/\alpha$ whereas the tangent stiffness is the derivative of the restoring torque $k_t = dM/d\alpha$, see [53, Fig. 4.3]. This is analogous for linear springs, see Eq. (1).

This results in a vertical shift of the force-displacement characteristic, as illustrated in Fig. 8. The sign of F_{gh} depends on the CG position with respect to the center of rotation. When the CG position is on the same side as the probe tip, force F_{gh} has a negative sign, because it is sensed in opposition to F as it causes rotation of the lever in the opposite direction.

Remark 1. Note that the orientation of the load cell with respect to gravity depicted in Fig. 7, which corresponds to the experimental setup, has been chosen to position the probe needle horizontally as is typical for micro- and nanoprobing.

3.2.2. *Effect of a vertical CG offset on the load cell*

The vertical component of the CG distance from the rotation axis, labelled d_v in Fig. 7, creates an effect analogous to a gravity pendulum (or an inverted pendulum): the gravitational potential energy of the lever either increases or decreases when rotating, depending on whether the CG is placed below or above the rotational axis, respectively (see [53, Sec. 6.4]). The change in the gravitational potential energy can be sensed at the probe tip as the force

$$F_{gv} = gm_{lev}\frac{d_v}{l_p}\sin(\alpha)\cong^{\alpha\approx 0}gm_{lev}\frac{d_v}{l_p l_r}x. \tag{12}$$

Observe that, for small rotations, this force is proportional to the probe tip displacement, which results essentially in a stiffness change. The sign of the stiffness change depends on whether the CG position is above the rotational axis (reduced overall stiffness) or below it (increased overall stiffness), as shown in Fig. 8.

3.2.3. *Parasitic shift of the center of rotation*

The parasitic shift of the rotation axis of the T-shaped flexure pivot for small deformations is depicted by $\overrightarrow{\lambda}$ in Fig. 7. It results from the shortening of the blades composing the flexures during their deformation. Therefore, $\overrightarrow{\lambda}$ can be broken down into two perpendicular vectors, one corresponding to the shortening of a longitudinal blade and the other related to the shortening of the transversal blade. The shortening of a single longitudinal blade equals $\frac{x_0}{2}$ and its analytical formula is given in [52, Eq. (13)]. The shortening of the transversal blade can be approximated as the parasitic shift of an RCC joint described in Ref. [54] for a special case with a zero angle between the blades. Finally, the expression describing the parasitic center shift of the TIVOT takes the form

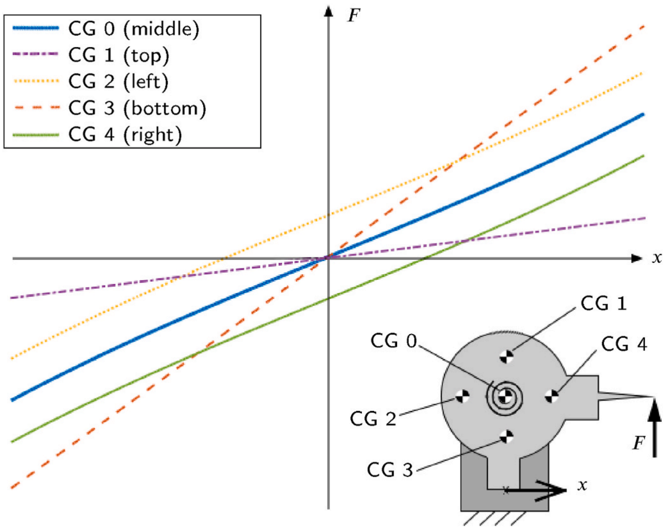

Fig. 8. A qualitative graph presenting the effect of five different positions of the CG (middle, left, right, top, bottom) on the force-displacement characteristic of the load cell.

$$\begin{aligned}|\overrightarrow{\lambda}| &= \lambda(x) = \sqrt{\left(\frac{9\frac{p^2}{\bar{l}}+9p+\bar{l}}{15}\alpha^2\right)^2+\left(\frac{x_0(\alpha)}{2}\right)^2} = \\ &\cong^{\alpha\approx 0}\sqrt{\left(\frac{9\frac{p^2}{\bar{l}}+9p+\bar{l}}{15l_r^2}x^2\right)^2+\left(\frac{x_0\left(\frac{x}{l_r}\right)}{2}\right)^2}.\end{aligned} \tag{13}$$

The potential energy change caused by this parasitic shift depends on the orientation of the mechanism, so we can express the associated force sensed at the probe tip as

$$F_{go}(x) = gm_{lev}\cos\left(\angle\left(\overrightarrow{g},\overrightarrow{\lambda}\right)\right)\frac{\mathrm{d}\lambda(x)}{\mathrm{d}x}. \tag{14}$$

For small rotations this force is proportional to the probe tip displacement, which results essentially in a stiffness change. Note that the parasitic shift of the center of rotation also occurs along the longitudinal blades affecting the measured output x. This effect, given by $x_0(\alpha)$, is however, negligible for such a small lever rotation.

3.2.4. *Overall effect of gravity on the load cell*

In summary, the overall influence of gravity on the mechanism is given by

$$F_{grav}(x) = F_{gh} + F_{gv}(x) + F_{go}(x). \tag{15}$$

We see that for a fixed orientation of the mechanism and for a given probe needle, one can find a CG position that minimizes the influence of gravity on the load cell. To achieve this, the horizontal CG shift must be zero ($F_{gh} = 0$) and the vertical CG shift chosen to minimize the expression $|F_{gv} - F_{go}|$. In case of a change in the orientation of the load cell or replacement of the probe needle, one can adjust the position of the CG with the ballast pins. Alternatively, since we showed that the effects are a combination of constant force offset and stiffness change, they can be compensated using the analytical model, the ZOT, and the stiffness adjustment mechanism.

3.3. *Zero offset tuning*

Zero offset means that the sensor output (lever position x) at zero input force is higher or lower than the ideal output. In other words, a non-zero force is measured when the lever is in contact with the sample at neutral position. This may result from limited manufacturing precision or changes in parameters of the load cell, e.g. from a change in the orientation of the mechanism or probe tip replacement. In order to control this offset, we introduced the zero offset tuning (ZOT) mechanism depicted in Fig. 9. One can use this mechanism to compensate for a horizontal CG offset described in 3.2.1, or to adjust the force measurement range.

The working principle of the zero offset tuning mechanism is generating a fixed torque M_{zot} around the rotational axis of the lever, by deforming the transversal blade. The deformation imposed is a rotation β about the midpoint of the transversal blade in order to minimize its internal stress, as demonstrated in Ref. [56]. This motion is achieved thanks to an RCC joint consisting of two blades placed on either side of the transversal blade and crossing virtually at its midpoint C. The dimensions of the RCC joint are not critical, but their selection affects the amount of force required for the adjustment and the admissible displacement. The adjustment range is relatively small ($x_{z\ max} \ll d$ in Fig. 9), hence the impact of ZOT on the kinematics of the load cell is negligible. The torque M_{zot} will result in a force

$$F_{zot}(x_z) = \frac{M_{zot}(x_z)}{l_p} = \frac{EI_t\beta(x_z)}{\bar{l}l_p}, \tag{16}$$

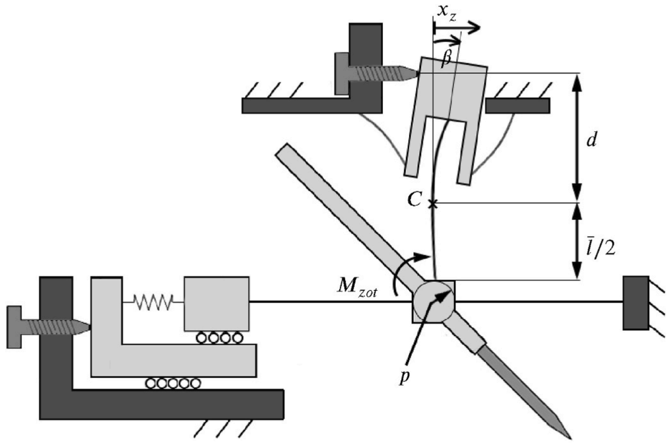

Fig. 9. Parametrization of the zero offset tuning mechanism. By applying displacement x_z we deflect the transversal blade by angle β, which results in reaction torque M_{zot} applied to the rotation axis of the lever.

at the probe tip, where

$$\beta(x_z) = \operatorname{asin}\left(\frac{x_z}{d}\right) \cong^{x_z \ll d} \frac{x_z}{d}. \tag{17}$$

The advantage of this mechanism is the continuity allowing setting the offset force with great precision limited only by the x_z adjustment precision, and the possibility of remote adjustment if an actuator, e.g. piezoelectric, is used. The zero offset tuning range is limited by the maximum admissible bending stress σ_{adm} in the transversal blade, corresponding to the maximum torque [28].

$$M_{zot\ max} = \frac{2I_t\sigma_{adm}}{h}. \tag{18}$$

It is important to consider an increased safety margin for the maximum internal stress of the transversal blade because the blade is subject to deformation by both the ZOT mechanism and the rotation of the load cell lever during operation.

It follows from the analytical developments of Sections 3.1-3.3 that the complete analytical formula for the force-displacement characteristic of the studied load cell is the sum of the forces resulting from the elastic deformation of the TIVOT during rotation of the lever, see Eq. (8), the influence of gravity, see Eq. (15) and the ZOT mechanism, see Eq. (16)

$$F\left(x, x_p, x_z\right) = F_{flexure}\left(x, x_p\right) + F_{grav}(x) + F_{zot}(x_z). \tag{19}$$

4. Load cell prototype design

4.1. Dimensioning of the mechanism

In addition to the force measurement requirements listed in Table 1, we defined particular specifications in order to ensure that the prototype is fabricable and practical for experimental validation of the presented concepts, see Table 2. We then used the analytical model to predimension the mechanism to satisfy these two sets of specifications, and the result can be seen in Table 3.

One of the challenges of dimensioning the prototype was to achieve a wide range of adjustable stiffness k_t, allowing measuring forces in the nanonewton to millinewton range in both positive and negative stiffness modes. In order to achieve this, it was necessary to provide a high compression load P_0 acting on the longitudinal blades. However, preliminary calculations showed that such a large force acting along the blades would buckle them and eventually damage the mechanism. For this reason, we reinforced the longitudinal blades by thickening their cross-section in the middle as shown in Fig. 10.

Table 2
Specifications related to the use of the force sensor prototype on the test bench.

Parameter	Symbol	Value	Comment
Material	–	Titanium Ti–6Al–4V (grade 5)	Good elastic properties, suitable for EDM and electrically conductive
Thickness	b	2 mm	High rigidity of the mechanism in directions other than the rotational DoF of the lever, preventing accidental damage during manipulation
Lever rotation range	α_{max}	±3° or more	Relatively large deflection for convenient testing and characterization
Output displacement resolution	Δx	$\leq 1\mu m$	Resolution offered by common displacement sensing technologies, such as laser-based displacement sensors
Preload spring maximum compression	$x_{p\ max}$	$\geq 1\ mm$	Relatively large stroke for convenient manual adjustment
Stiffness adjustment range	k_t	±50 N/m or more	Positive stiffness ensuring the assumed measurement range F_{max}, possibility to achieve a near-zero stiffness and a symmetrical negative stiffness range for testing the bistable mode
ZOT maximum stroke	$x_{z\ max}$	±1 mm or more	Relatively large stroke for convenient manual adjustment
ZOT range	$F_{zot\ max}$	±10 mN or more	Corresponds to approximately one-third of the maximum force measuring range

Table 3
Dimensions of the load cell prototype.

Part	Symbol	Description	Value
Longitudinal blades	$\tilde{l}$	length	6.1 mm
	$\tilde{l}_{eq}$	equivalent length	6.6 mm
	$\tilde{h}$	width	0.1 mm
	a	thickening	2 mm
Transversal blade	$\bar{l}$	length	9 mm
	$\bar{h}$	width	0.167 mm
Preload spring stage	l	length	26 mm
	h	width	1.05 mm
	n	number of parallel blades	2
ZOT RCC joint		blade length	12 mm
		blade width	0.2 mm
	d	lever length	18.5 mm
Lever	l_p	probing distance (incl. a 32 mm probe)	48 mm
	l_r	reflector distance	18 mm
	p	center radius	1.8 mm
Material	E	Young's modulus	114 GPa
	σ_{adm}	yield strength divided by the safety factor of 1.6	518.75 MPa

This modification, has an impact on the stiffness and on the admissible deflection of the T-shaped joint. In order to be able to use the model described in Eq. (6), which assumes blades with uniform cross-section, we found an equivalent length $\tilde{l}_{eq}$ for these "theoretical blades" which would render their behavior equivalent to the reinforced blades that are actually used in the prototype. We did this by comparing the analytical formulas for the stiffness and admissible deflection of RCC pivots constituted of flexures with uniform cross-section [28] and with reinforcement [57], see Fig. 11. The equivalent blade length $\tilde{l}_{eq}$ could then be found from the graph, based on either having an equivalent stiffness or an equivalent admissible deflection. In this article, we used the

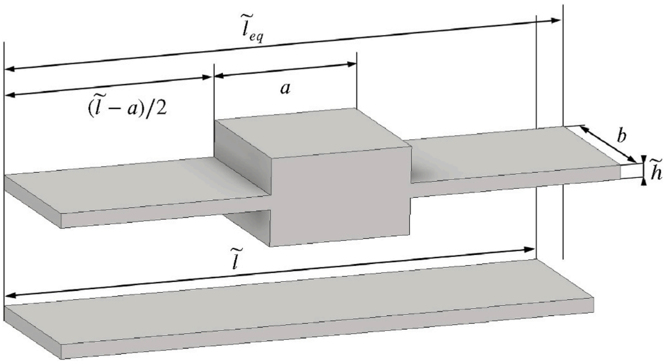

Fig. 10. Parametrization of longitudinal blade dimensions and equivalence between the longitudinal blades with and without thickening in the middle.

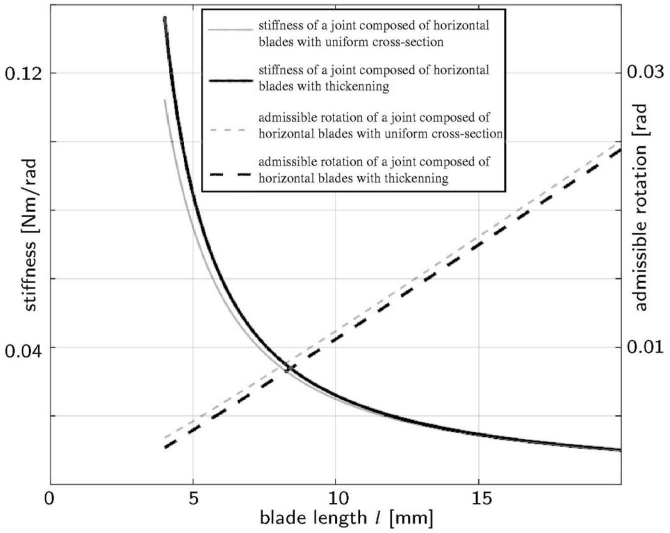

Fig. 11. Comparison of stiffness and admissible deflection obtained analytically for an RCC pivot consisting of two blades with [57] and without [28] reinforcement. Dimensions $\widetilde{h}, a$ specified in Table 3 were used.

second criterion as it gave better results and guaranteed an identical range of movement of the mechanism.

The transversal blade did not require reinforcing as it is not subject to compressive forces. However, the transverse blade has different dimensions than the longitudinal ones to reach a higher stiffness, thus enhancing the range of zero offset tuning.

4.2. Numerical validation

We illustrate the FEM model of the prototype in Fig. 12. It was developed to validate the correctness of the analytical model and to validate the pre-dimensioning by investigating the internal stresses occurring in the mechanism over its entire operating range. We performed the simulations in COMSOL 5.5, considering the geometric nonlinearities.

A variable mesh was used in the simulation, with the minimal element size of 0.025 mm for the blades arranged in T shape, corresponding to maximally 1/4 of their width, and with the maximal element size of 9 mm for the fixed frame of the mechanism. The minimal element sizes of stiffness adjustment preload and zero offset mechanisms were 0.2 mm and 0.04 mm respectively.

The simulations showed that, while deflecting the lever along its rotational DoF, the maximum internal stresses occur in the longitudinal blades. Their analysis showed that in the worst case, depicted in Fig. 12, the stress is below σ_{adm} so there is no risk of their breaking in normal functioning of the mechanism. Moreover, the application of a transverse force acting on the end of the lever shows a resistance of the mechanism to forces above 3 N, which meets the requirements given in Table 1.

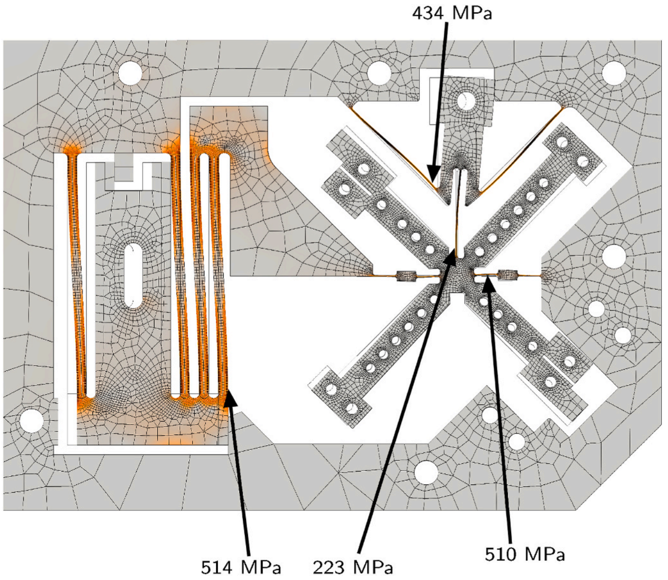

Fig. 12. FEM simulation performed on the load cell mechanism. The presented configuration is the case with the greatest internal stress at $x_p = x_{p\ max}$, $\alpha = \alpha_{max}$, $x_z = x_{z\ max}$. The shading indicates the parts of the mechanism where internal stress occurs. The arrows indicate the points at the lateral surfaces of the beams, at which the maximum von Mises stress occurs.

We also used the simulations to plot the force-displacement characteristics as a function of the stiffness adjustment displacement x_p and zero offset tuning x_z. We compared the obtained results with the analytical model and the experimental results in section 5.

4.3. Probe needle replacement

The differences among electrical micro- and nanoprobing applications, as well as the ease of damaging the probe needle during micromanipulation, make the possibility of probe replacement one of the key requirements of the designed load cell. The load cell prototype provides a lot of flexibility in the design of the probe holder, thanks to its mesoscale design. Additionally, the relatively large thickness of the mechanism (2 mm) results in high stiffness along its degrees-of-constraint that protects the mechanism against accidental damage during the manual replacement of the probe needle.

The probe holder itself is out of the scope of this study, but the simple design used in the prototype (Fig. 13) constitutes an example of a solution that allows manual probe needle replacement. If the replaced probes differ in weight or dimensions, it may shift the center of gravity of the lever. To prevent this, we can adjust the position of the CG using the system depicted in Fig. 14. The lever of the load cell is designed to be symmetrical about the axis of rotation (3). For this reason, we mounted the probe holder (4) with the corresponding element on the opposite side of the lever (1) and the reflector (7) for the output displacement laser beam (6) with the counterweight (2) on opposite ends of the lever. We can compensate for the weight of the probe needle (8) by inserting ballast pins (5) into holes located on the two perpendicular axes of the lever. The same pins can be used to adjust the CG position in the plane of the mechanism, which can have interesting properties, see Sec. 3.2. In addition, we can compensate the weight of the probe needle with the stiffness adjustment and ZOT mechanisms, see Sec. 3.2 or by mounting an identical end effector on the opposite side of the lever (1).

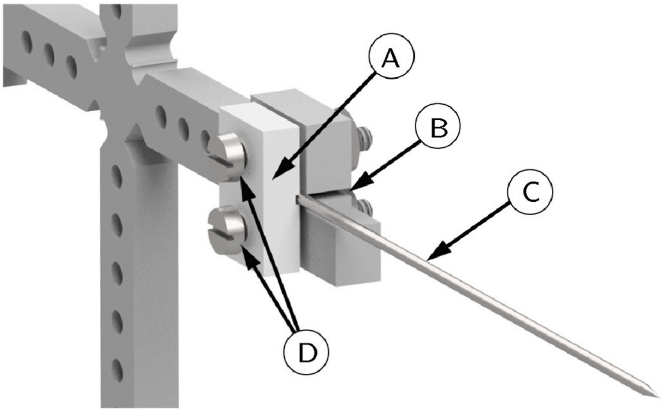

Fig. 13. The simple probe holder used during the experiments, allowing exchange of various probe needles dedicated to electrical micro- and nanoprobing. Marked elements: A - polymer probe needle clamp, B - probe needle guiding slot, C - probe needle, D - two locking screws.

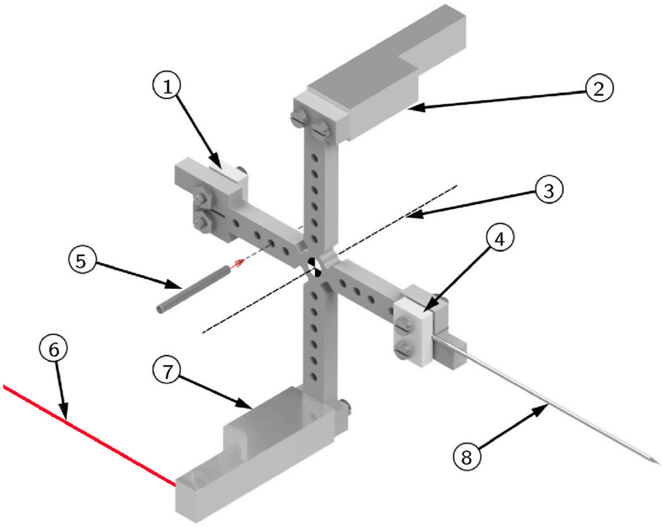

Fig. 14. A schematic of the lever assembly. To improve clarity, the blades on which the lever is suspended are not shown.

5. Experimental validation

This section characterizes the load cell prototype experimentally. By measuring the static force-displacement characteristic of the load cell, we can validate the stiffness adjustment and zero offset tuning mechanisms, as well as the different working modes (positive and negative stiffness). Additionally, we use the results to validate the analytical and FEM models developed in Sec 3 and 4.2 respectively.

5.1. Experimental setup

In order to obtain the force-displacement characteristic of the prototype for different values of tuning displacements x_z and x_p, we developed the test bench shown in Fig. 15. The input force F applied to the probe tip is measured using a reference force sensor (FUTEK FSH03395) with an accuracy of ±75 μN, controlled by displacing this sensor with a nanopositioning stage (PI Q522). To provide sufficient range of motion, the stage is controlled in coarse (stick-slip) mode with an accuracy of approximately 0.5 μm. We used a weight compensation for the reference force sensor to facilitate the movement of the nanopositioning stage.

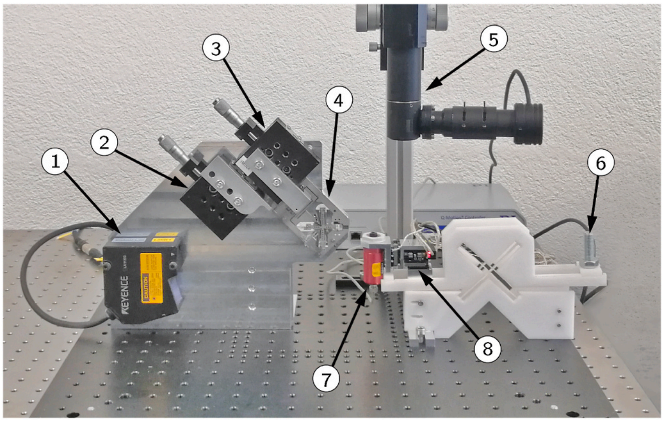

Fig. 15. The test bench used for characterization of the new load cell. Marked elements: 1 - laser displacement sensor, 2 - micropositioning stage for zero offset tuning, 3 - micropositioning stage for stiffness adjustment, 4 - tested mechanism, 5 - microscope, 6-wt compensation for the reference force sensor, 7 - reference force sensor, 8 - nanopositioning stage.

The force measurement resolution of the load cell is not limited by the number of bits of the read-out system but by the smallest detectable displacement change. In the setup used, the output displacement x was measured with a laser displacement sensor (LK-H152) whose smallest detectable displacement is $R_d = 0.1$ μm, and within the operating region, its accuracy was determined as $+2/-3$ μm. The tuning displacements x_z and x_p of the stiffness adjustment and zero offset tuning mechanisms are applied using manual micropositioning stages with an accuracy of around 1 μm. The stages are connected to the mechanism in a way that avoids hyperstatism so as not to affect the performance. Finally, the position of the probe tip is visually assessed using a microscope.

We made all measurements using a 38 mm-long probe tip, except when testing different probe tip lengths (Fig. 22). In order to increase the accuracy of the measurements, the fixed frame of the prototype was assembled on an optical table with passive vibration isolation. As the goal was to measure the static force-displacement characteristic $F(x)$, we performed the measurements on a stabilized mechanism to prevent dynamic effects.

5.2. Stiffness adjustment

In order to validate the stiffness adjustment concept of the load-cell, we measured its force-displacement curves for different values of the preload displacement x_p. When the preload exceeds a certain value, the stiffness becomes negative and the system switches from monostable mode ($k_t(0) > 0$) to bistable mode ($k_t(0) < 0$). These two modes require different measurement procedures detailed in Sections 5.2.1 and 5.2.2.

5.2.1. Positive stiffness

When the stiffness of the load cell is positive, e.g. when there is no preload, the lever has one stable position (nominal position) from which it is deflected when an external force is applied on the probe tip. The procedure used to measure its force-displacement curve consists of three phases depicted in Fig. 16:

A1 The lever is in neutral position. The reference force sensor is below it and moves up, towards the probe tip.

A2 The reference force sensor meets the probe tip and continues its upward motion, increasing the contact force and lever deflection. The mechanism is stabilized before a measurement is taken.

A3 After reaching the predefined maximum deflection, the reference force sensor moves in the opposite direction until it loses contact with the probe tip

The resulting force-displacement curves for three different values of

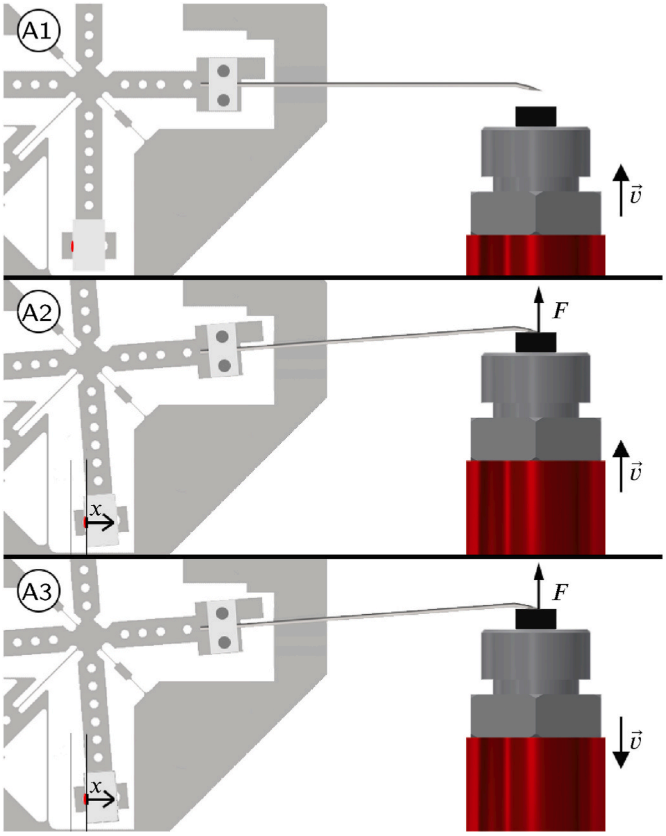

Fig. 16. Procedure for determination of the positive stiffness force-displacement characteristic.

preload displacement x_p are shown in Fig. 17. One can see that increasing the preload decreases the slope of the force-displacement curve, i.e., the stiffness, allowing tuning. Of note, we also display numerical and analytical results.

5.2.2. Negative stiffness

When the stiffness of the load cell is negative ($k_t(0) < 0$), the mechanism works in bistable mode. In this case, there are two stable positions of the lever (typically, the two extreme positions). To start deflecting the lever, one must apply a sufficient initial force to overcome the restoring force of the T-shaped pivot in its stable position. This initial force is referred to as the threshold force, see Fig. 18. After reaching the threshold force, the restoring force decreases (due to the negative stiffness) up to a point where the lever suddenly transits to the second stable position. Qualitative curves of input force F and output displacement x during probe landing in bistable mode are depicted in Fig. 18.

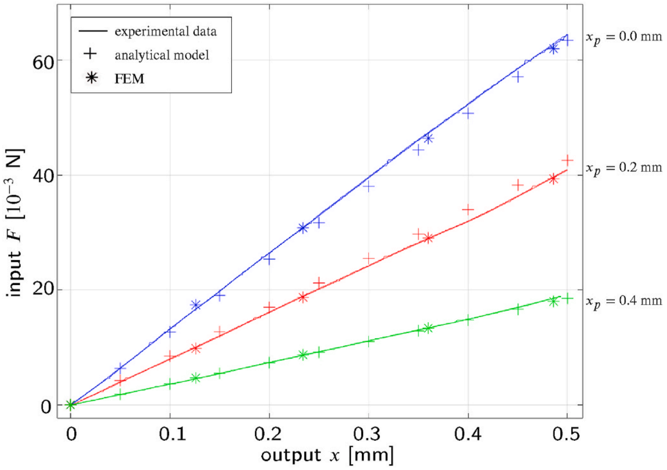

Fig. 17. Graph presenting several force-displacement curves within the region of positive stiffness. Comparison of experimental data with the analytical results given by Eq. (19) and FEM simulation.

The procedure used to measure the force-displacement curve of this bistable system consists of three steps depicted in Fig. 19:

- B1 The mechanism operates in a bi-stable mode, therefore, the lever is initially in the extreme down position. The reference force sensor is below and moves up, towards the probe tip.
- B2 The reference force sensor meets the probe tip and continues to move upwards. Once the threshold force is surpassed, the mechanism lever rotates towards the neutral position. The mechanism is stabilized before a measurement is taken.
- B3 While crossing the neutral position, the lever suddenly transits to the extreme high position and loses contact with the reference force sensor.

We show the resulting force-displacement curve for four different values of preload displacement x_p in Fig. 17. One can see that, for these values of the preload displacement, the slope of the force-displacement curve, i.e., the stiffness, becomes negative. The preload displacement is higher than for the monostable mode (Fig. 16) and adjusting it allows varying the stiffness again. Note that we also display numerical results but not the analytical results as the model does not precisely describe the negative stiffness behavior.

5.2.3. Stiffness tuning precision

In order to provide numerical data for the stiffness of the load cell, we used the tangential stiffness $k_t(0)$ obtained by deriving the force-displacement curve around its nominal position. This value is particularly relevant for micromanipulation applications, where deformations typically do not exceed microscopic range. Fig. 21 depicts the resulting stiffness tuning curve for varying the preload displacement obtained experimentally, numerically and analytically. One can see that the relationship is linear, with a tuning precision (slope) of 0.233 N/m per μm.

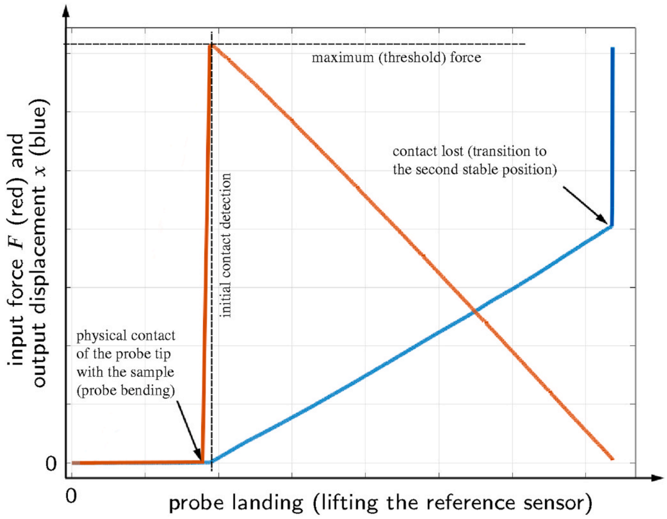

Fig. 18. A qualitative graph showing a typical simultaneous force and displacement measurement for a load cell operating in the negative stiffness range (bistable mode). The force measurements take place after the initial contact is detected.

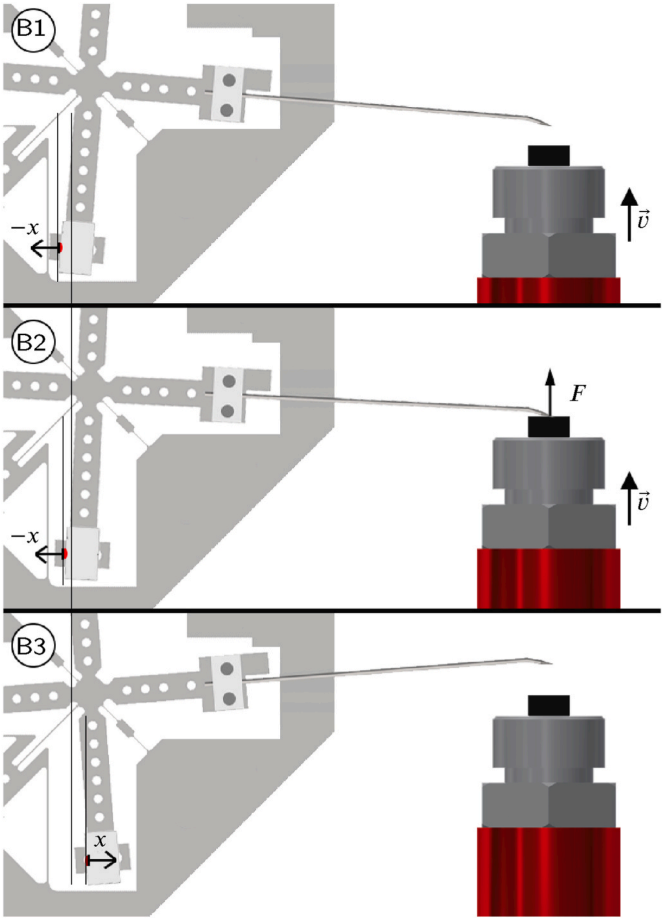

Fig. 19. Procedure for determination of the force-displacement characteristic measured at negative stiffness.

5.2.4. *Summary*

Overall, the results of this section enable us to conclude that:

- The stiffness adjustment mechanism is an effective way of accurately controlling the stiffness of the load cell by acting on the displacement x_p.
- The mechanism achieves the two working modes of interest (positive and negative stiffness).
- The negative stiffness (bistable) working mode is a practical way of setting a threshold force that protects the sample and probe against damage. Indeed, the maximal force can be controlled and it only decreases after contact.
- To the precision of the sensors used in the experimental setup, no hysteresis was observed in the operation of the load cell.
- The numerical model accurately predicts the stiffness behavior over the entire tuning range.
- The analytical model accurately predicts the stiffness behavior for positive stiffness values.
- With a maximum force of 64.4 mN measured by the load cell in positive stiffness mode ($x_p = 0$) and a maximum force of 29.3 mN in negative stiffness mode ($x_p = 0.75$ mm), the device satisfies the ±20 mN measurement range specification of Table 1 for both modes. Note that the negative force range corresponds to operation on the other side of the neutral position, assuming symmetrical behavior.

One can see that the analytical results diverge from the experimental and FEM results as the preload increases, in particular in the negative stiffness range. This can be explained by the use of reinforced longitudinal blades in the physical device, whereas the analytical model assumes blades with a constant cross-section, see Fig. 10. At near zero stiffness ($x_p = 0.55$ mm), the analytical model returns a 6.36% discrepancy from the measured stiffness, which is acceptable for pre-dimensioning.

Remark 2. In the large positive and negative stiffness ranges shown in Figs. 17 and 20, the force-displacement characteristic is highly linear. This is not the case when the mechanism has near-zero stiffness but this case will be treated in section 5.4 because it requires prior characterization of the zero offset tuning mechanism described in 5.3.

Remark 3. The negative stiffness characteristic can only be measured until transition to the second stable state, see Fig. 16. Fig. 20 shows that this transition occurs around the nominal position.

Remark 4. The length of the probe needle also affects the overall stiffness of the load cell by changing the lever arm of the probing force (see parameter l_p in Eq. (10)). This effect, shown in Fig. 22, can be used to offset the stiffness range. Alternatively, when probe needles of different lengths are used, this effect can be compensated by using the preload setting x_p to maintain the same load cell properties.

5.3. *Zero offset tuning*

The purpose of the ZOT mechanism is to apply a constant torque on the load cell so as to create a constant offset on its measurement output, i.e., offset its force displacement curve. The force-displacement curves in Fig. 23, measured for 8 values of the tuning parameter x_z, show that the prototype successfully realizes this feature.

In order to guarantee that this feature is proper tuning, we show that it does not affect other crucial properties of the load cell. First, Fig. 23 shows that the stiffness of the load cell (the slope of the curve) is not significantly affected by the tuning. Secondly, Fig. 24 shows that the force offset (at nominal displacement $x = 0$) for different values of tuning displacement x_z is independent of the stiffness adjustment parameter x_p.

Fig. 24 also shows that the experimental, numerical and analytical results match. The zero offset tuning follows the linear characteristic described in Eq. (16) (for small adjustments x_z) with a precision of 13.6 N/m. The tuning range of the ZOT is at least $\pm 10 \cdot 10^{-3}$ N, which is enough to compensate the weight of different end effectors specified in Table 1.

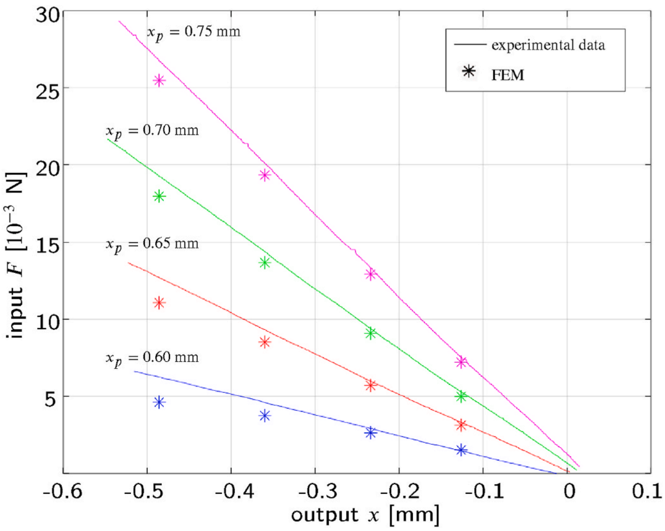

Fig. 20. Graph presenting several force-displacement curves within the region of negative stiffness. Experimental and FEM results are displayed.

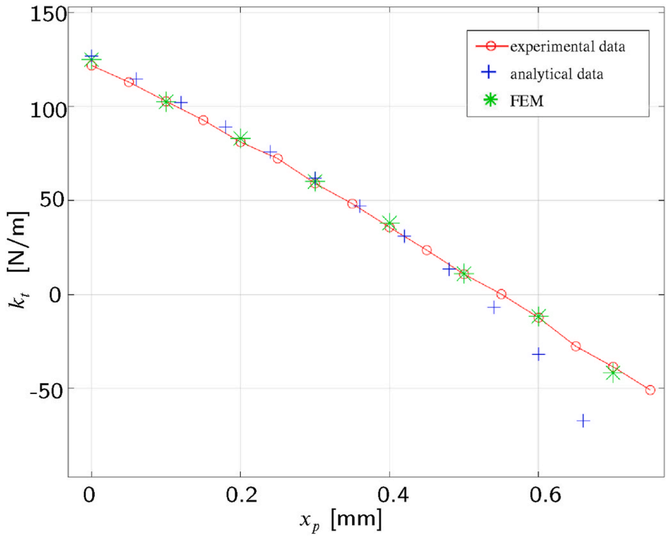

Fig. 21. Graph presenting the overall stiffness of the mechanism $k_t(0)$ as a function of stiffness adjustment displacement x_p. Experimental results are compared with the analytical model given by Eq. (10) and FEM simulation.

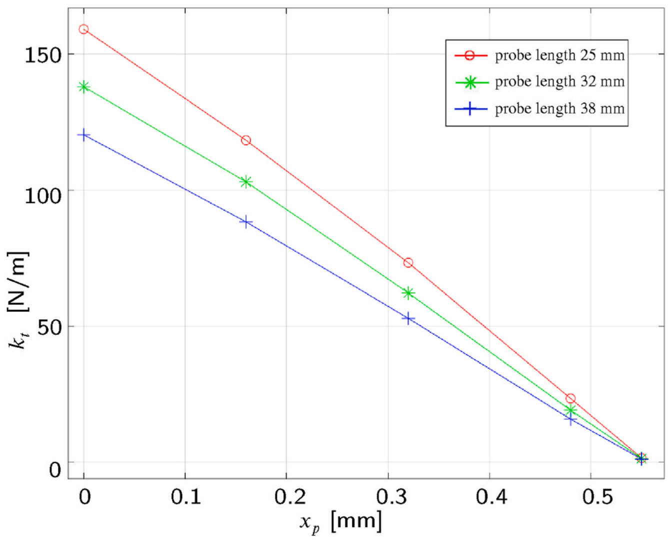

Fig. 22. Graph presenting the overall stiffness adjustment using the preload displacement x_p for three different probe tip lengths. Data obtained experimentally.

5.4. Sensitivity and dynamic range

The force-displacement characteristic in the near-zero stiffness range ($x_p \approx 0.55$ mm) is presented in Fig. 25 for different values of the stiffness tuning parameter x_p. Note that a constant force offset $0.53 \cdot 10^{-3}\ N$ was applied using the ZOT mechanism in order to measure the characteristic for the full range of the output displacement x.

One can see that a value can be found where the stiffness around $x = 0$ is practically null. Indeed, the measured stiffness for $x_p = 0.55$ mm) is $k_t(0) = 0.101$ N/m, which is a 1206 fold decrease compared to the stiffness of $k_t(0) = 121.8$ N/m measured without stiffness tuning ($x_p = 0$ mm, see Fig. 17). Note that the near zero stiffness characteristic is highly non-linear, which prevents achieving constant overall stiffness within the entire workspace. In case the force measurements are made in the micrometer range, these non-linear effects can be neglected. Otherwise, the non-linear characteristic is actually of advantage as it increases the virtual dynamic range of the sensor, as discussed below.

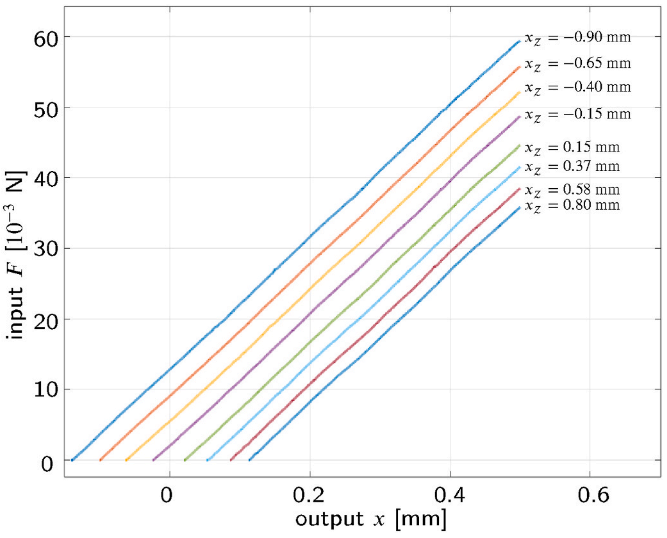

Fig. 23. Graph presenting the force-displacement characteristic offset obtained for several zero offset tuning adjustments x_z. Data obtained experimentally at $x_p = 160$ µm.

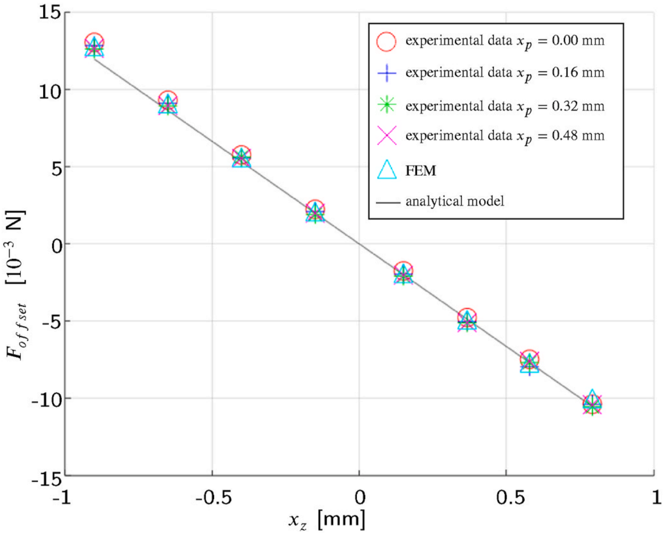

Fig. 24. Graph presenting the force-displacement characteristic offset as a function of zero offset tuning displacement x_z. Experimental data show a good agreement with the analytical model and the FEM.

5.4.1. Measurement sensitivity

The near-zero stiffness behavior of the load cell is of great interest as it improves the force sensing resolution and increases the sensitivity of the device. Force sensing resolution $R(x)$ for the new load cell is given by

$$R(x) = R_d k_t(x), \tag{20}$$

where $R_d = 0.1$ µm, see Sec. 5.1. Defining the resolution helps to analyze the results obtained by the physical device. On the other hand, sensitivity defined as

$$s(x) = \frac{1}{k_t(x)}, \tag{21}$$

is the crucial characteristic of our device as it defines the measurement resolution without depending on the choice of displacement sensor. In theory, if we approach zero stiffness, the sensitivity tends towards infinity, i.e., the measurement resolution tends towards zero ($R(x) \to 0$). In

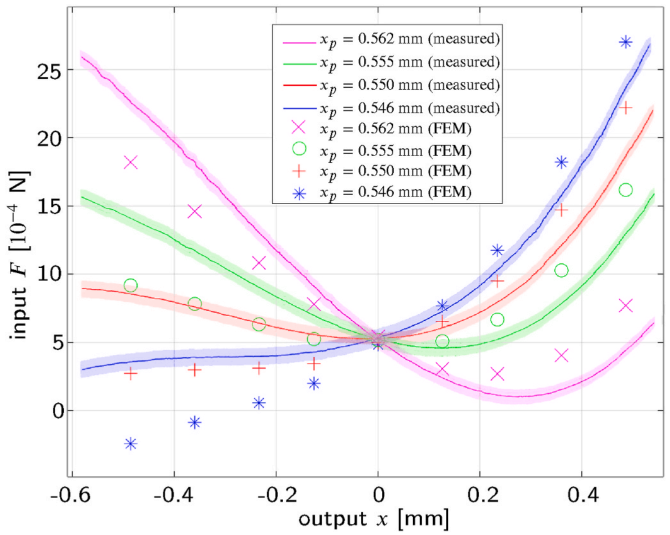

Fig. 25. Graph presenting several force-displacement curves near zero stiffness. The shaded regions of confidence presented in the graph correspond to the inaccuracy of the sensors used in the experimental setup. Comparison of experimental data with FEM simulation.

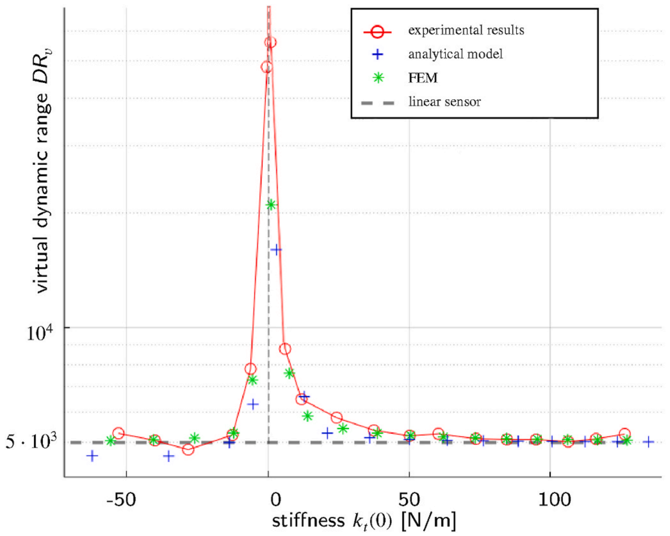

Fig. 26. Virtual dynamic range with respect to load cell stiffness. The large increase in DR_v near zero stiffness results from the increase in non-linearity of the force-displacement characteristic and is beneficial for micro- and nanoprobing.

practice, with a stiffness of $k_t(0) = 0.101$ N/m, the sensitivity was increased by a factor of 1206 compared to the case without stiffness tuning and we achieved a resolution of $R(0) = 10.1$ nN. This value considerably exceeds the $< 500\,nN$ specification of Table 1 and, in terms of resolution, puts this sensor on a par with state-of-the-art micro-scale solutions such as [26,27].

5.4.2. Dynamic range

We define the dynamic range DR of a sensor as the ratio between the maximum and minimum signal that is acquired. For micromanipulation applications, this is an important characteristic as forces with high variations in magnitude can occur. A high dynamic range allows detecting large forces, for instance when meeting the sample, while being able to perform very precise operations (small forces).

For a sensor with a linear force-displacement sensor characteristic, the dynamic range is a constant defined by the resolution of the displacement sensor and the maximum measured displacement

$$DR = \frac{k_t(0)x_{max}}{R(0)} = \frac{x_{max}}{R_d}. \tag{22}$$

By having a non-linear force-displacement characteristic, the dynamic range of the sensor is increased. Indeed, one can see in Fig. 25 that the slope of the force displacement curve changes, allowing measuring forces of the order of 0.001 N while having a high sensitivity (near-zero stiffness) in the micromanipulation range (around $x = 0$). We hence introduce the notion of virtual dynamic range

$$DR_v = \frac{F_{max}}{R(0)} = \frac{F_{max}}{R_d k_t(0)} \tag{23}$$

where F_{max} is the absolute value of the largest force measured over the measurement range $\pm\, x_{max}$ (within a given stiffness adjustment) and is greater than $k_t(0)x_{max}$. Using this definition, we show the virtual dynamic range of our prototype as a function of its stiffness in Fig. 26. One can observe that the dynamic range in the near-zero stiffness (high sensitivity) range is significantly increased in comparison to linear sensors. Bear in mind that the dynamic range of linear sensors is constant and that the maximum force measured with near-zero stiffness would hence be much smaller.

According to Eq. (23), the DR_v could in theory be infinite, if zero stiffness is achieved. In practice, with the near-zero stiffness setting $x_p =$ 0.55 mm, we reached $DR_v = 218 \cdot 10^3$, see Table 4. This represents more than 40 times the value measured at $x_p = 0$. Note that this result is not displayed in Fig. 26 to keep the plot readable. This value is of the same order as existing micro-force sensors [24] and we can still increase it by improving the stiffness adjustment (e.g. with a piezo actuator instead of doing it manually) or by using a displacement sensor with a higher resolution (e.g. capacitive or interferometry-based).

In the case where we apply stiffness adjustment during the measurement, for instance by controlling the displacement x_p with a linear piezo actuator, we could use both the maximum force corresponding to $x_p = 0$ and the maximum resolution obtained with $x_p = 0.55$. As a result, we would obtain a virtual dynamic range $DR_v = 6376 \cdot 10^3$, which is one order of magnitude better than most known micro-force sensors [24, 25], see Table 4. Note that this kind of sensitivity adjustment is common in state-of-the-art devices, as seen in Sec. 1.4.3.

Remark 5. The consistency of the performed measurements with the FEM results (only a slight constant slope offset in Fig. 25) demonstrates that FEM is an effective method for designing the mechanism as per specifications. The analytical model is less precise but seems to be an effective way of achieving an initial dimensioning of the mechanism.

Remark 6. Note that the restoring force is asymmetric in the near-zero stiffness range (Fig. 25). We can attribute this to the asymmetrical deformation of the transverse blade, already loaded by the ZOT mechanism and the deflection of the preload stage caused by the shortening of the longitudinal blades during the rotation of the lever, as seen in Fig. 12.

5.5. Impact of gravity on the load cell

The goal of this experimental part was to validate our analytical

Table 4
Virtual dynamic range DR_v of the prototype for different stiffness adjustments.

Stiffness adjustment	$F_{max}(N)$	$R(0)(N)$	DR_v
$x_p = 0$	$64.4 \cdot 10^{-3}$	$12.18 \cdot 10^{-6}$	$5.24 \cdot 10^3$
$x_p = 0.55$ mm	$2.2 \cdot 10^{-3}$	$10.1 \cdot 10^{-9}$	$218 \cdot 10^3$
Start with $x_p = 0$ and tune to $x_p = 0.55$ mm	$64.4 \cdot 10^{-3}$	$10.1 \cdot 10^{-9}$	$6376 \cdot 10^3$

predictions for the impact of the lever's CG offset from the rotation axis on its force-displacement characteristic. At the same time, we showed that these effects can be cancelled using the two adjustment mechanisms of the device (stiffness adjustment and ZOT).

According to the analytical model of Sec. 3.2, the effect of the CG offset can be broken down into two effects resulting from the horizontal and vertical components of the offset. We tested this hypothesis by inserting ballast pins into the lever to artificially offset the CG position, and measuring the force-displacement characteristic (Fig. 27).

5.5.1. *Impact of horizontal CG offset*

We show the measured force-displacement characteristics for two horizontal CG offsets (left and right positions in Fig. 27) and without ballast in Fig. 28. In order to highlight the effect of the offset, the result without ballast was subtracted from the two curves with ballast, shown in Fig. 29. The measured effect matches the constant force offset predicted by the analytical model with an average difference of 5.07% and a maximum difference of 12%. It is close to the $\pm 116 \cdot 10^{-6}$ N force predicted by Eq. (11), with ballast of $59 \cdot 10^{-6}$ kg at a distance of ±11 mm from the axis of rotation. Note that the force measured in the neutral position without ballast is non-zero because of the weight of the probe tip.

5.5.2. *Impact of vertical CG offset*

Contrastingly, Fig. 30 shows the force-displacement characteristics measured for two vertical CG offsets (top and bottom positions in Fig. 27) and without ballast. In order to highlight the stiffness (i.e. slope) change caused by the offset, the curves were derived and the result without ballast was subtracted from the results with ballast, see Fig. 31. One can see that the measured stiffness change is close to the constant +0.308 N/m and −0.969 N/m over the entire operating range predicted by Eqs. (12) and (14) with a pin at the bottom and top positions, respectively. The average difference between the measured and predicted values is 6.02% and the maximum difference is 16%. The $4.77 \cdot 10^{-3}$ kg ballast pins were placed at a distance of ±13.5 mm from the axis of rotation.

Observe that the slope change is asymmetrical with respect to the case without ballast (i.e. the change is greater when the ballast is in the top position). This is due to the increased effect of the parasitic shift caused by the increase in mass of the lever when adding the ballast, see Eq. (14). We thereby also validate this component of the analytical model. Note that the weight used to measure the effect of a vertical shift was 81 times greater than to measure the effect of a horizontal shift. This was necessary since, as predicted by the analytical model, the vertical CG shift has a significantly smaller impact on the force-displacement characteristics than the horizontal shift.

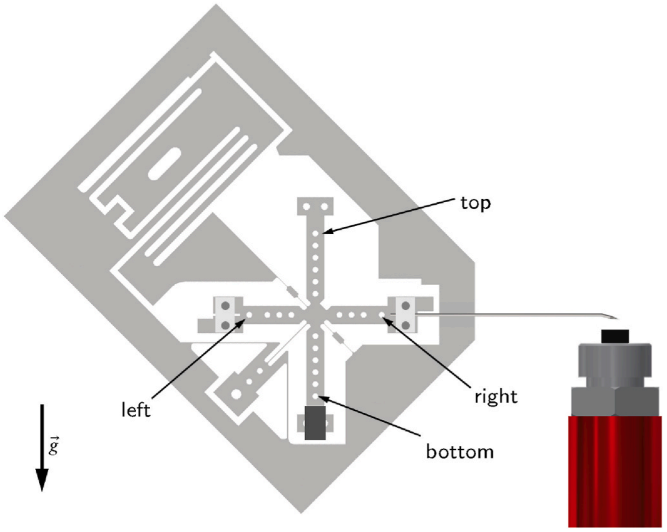

Fig. 27. Orientation of the mechanism during the measurements in relation to gravity. Positions in which ballasts were placed to change the position of the CG are indicated by arrows.

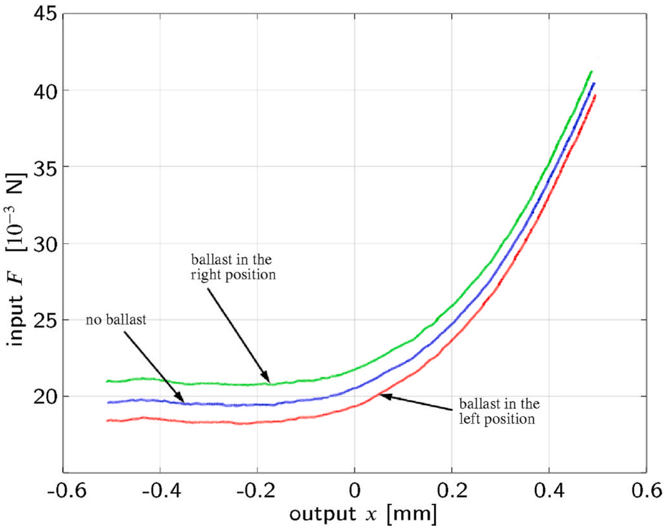

Fig. 28. Impact of the horizontal CG shift on the force-displacement characteristic. Measurements performed at $x_p = 548$ μm and $x_z = -150$ μm.

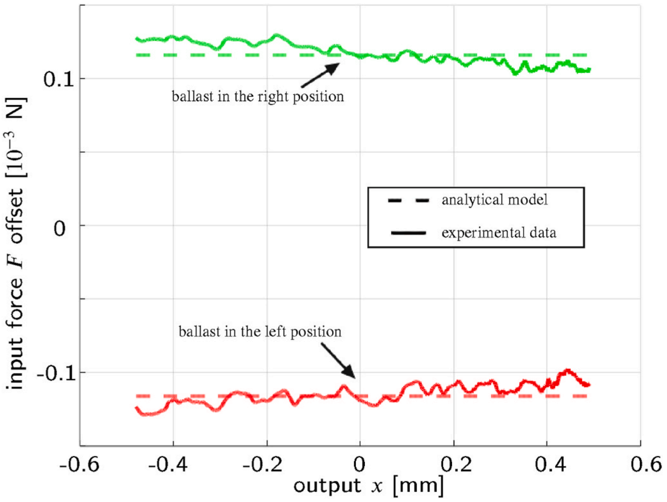

Fig. 29. Offset of the input force F obtained by subtracting the force-displacement characteristic without ballast in Fig. 28 from the ones with ballast. Analytical results are also displayed.

5.5.3. *Summary*

We were able to observe the effects of horizontal and vertical shifts of the CG on the force-displacement characteristic of the sensor. Since these effects correspond respectively to a nearly constant force offset and a nearly constant stiffness change, they can be compensated using the stiffness and zero offset tuning mechanisms validated previously. The analytical model provides a good estimation of these effects and can hence be used to implement the desired compensations. Note that the ballast pins should be used to provide a first level of CG position tuning. Indeed, positioning the CG on the axis of rotation will also be beneficial in terms of limiting the influence of orientation on the sensor's operation as well as potentially improving dynamic properties.

Remark 7. As a result of the large weight of the ballast pins used for the vertical offset measurement and their relatively low horizontal

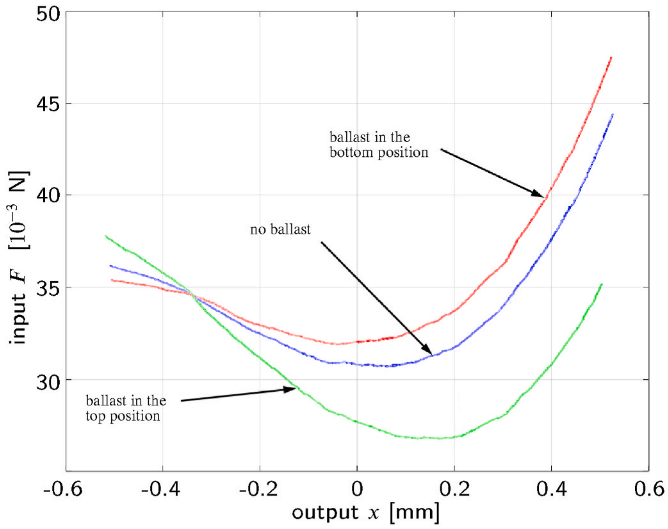

Fig. 30. Impact of vertical CG shift on the force-displacement characteristic. Measurements performed at $x_p = 550$ μm and $x_z = -225$ μm.

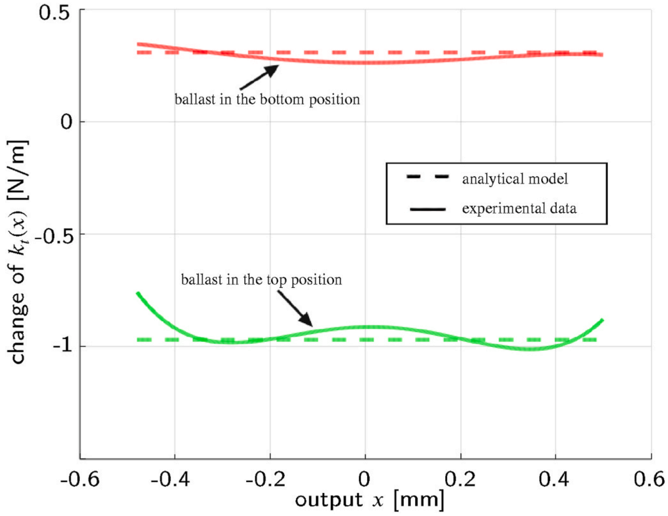

Fig. 31. Change of stiffness $k_t(x)$ obtained by deriving and subtracting the force-displacement characteristic without ballast in Fig. 30 from the ones with ballast. Analytical results are also displayed.

positioning precision of about ±0.5 *mm*, an unforeseen force offset can be observed between the measured curves in Fig. 30. This does not affect the overall stiffness of the lever (only the vertical component of the offset does) and can be compensated with the ZOT mechanism. However, an increased precision in the positioning of the CG could be beneficial for further prototypes.

6. Contributions and conclusion

To summarize, the main contributions of this article are:

- A novel flexure-based load cell design, whose measurement range and sensitivity can be adjusted and whose end effectors can be exchanged in order to suit a variety of micro- and nanoprobing applications.
- Experimental validation of a T-shaped flexure pivot whose stiffness can be adjusted via a preload and which can reach near-zero or negative stiffness. The negative stiffness (bistable) behavior allows for safe probing, protecting the probe and sample from overload.
- A mechanism enabling adjusting the zero offset (nominal force) of the load cell (and hence tune the measurement range) without significantly affecting the other properties.
- An analytical model enabling predicting the effect of gravity on the properties of the load cell and compensating for it. This can also be used to calibrate the device for various end effectors.
- Analytical models for the stiffness and zero offset tuning systems that were used to pre-dimension the system and can be used to predict the effect of the tuning.
- A finite element model that was used to precisely dimension the system and validate the design.
- Experimental validation of the design, the tuning mechanisms, the numerical model and the analytical models.
- A mesoscale physical load-cell prototype made of Ti–6Al–4V alloy reaching practical micro- and nanoprobing specifications. This prototype achieved a high measurement resolution of the order of 10 nN while having a dynamic range $DR_v = 218 \cdot 10^3$ (potentially $DR_v = 6376 \cdot 10^3$ with tuning during measurement) which is 40 times larger than a linear sensor with the same sensitivity.

Compared to our previous work [34], the structure of this sensor is simpler (less flexible parts), we model the effect of gravity and can compensate for it, and we reduce the dimensions of the prototype. We designed the prototype at the mesoscale to facilitate manipulation but, thanks to a compliant structure that does not require assembly, the device is suitable for microfabrication in materials such as glass [58] or silicon [59], which can considerably reduce its size.

It is worth noting that due to the use of flexible joints, the lever is exposed to oscillations that may affect the precision of the force measurement. This did not come into play in our experiments since we focused on static measurements for which the device performed as intended. Nevertheless, the use of ZOT and stiffness adjustment mechanisms can influence the dynamic properties of the device and may constitute an entry point for further research on its dynamic characteristics. Future work will also include enhancing the sensitivity of the load cell and validating the sensor in electrical micro- and nanoprobing with particular emphasis on the automation of the probe landing process.

Finally, the thermal sensitivity of the measurements will have to be investigated. Overall, we expect the thermal expansion to have an effect on the force-displacement characteristic of the load cell, but this effect should be mitigated by our monolithic design thus not changing the main principle of operation. Ideally, zero and stiffness adjustments should be made at the temperature at which the device is used to eliminate most thermal errors. Nevertheless, solutions using materials with low changes in elasticity and dimension due to temperature or compensating changes could be considered [60].

Declaration of competing interest

The authors declare that they have no known competing financial interests or personal relationships that could have appeared to influence the work reported in this paper.

Acknowledgments

The authors would like to gratefully acknowledge the financial support from the European Union’s Horizon 2020 research and innovation program under the Marie Skłodowska-Curie grant agreement No 722176). Moreover, the authors thank Hubert Schneegans for his important contribution in the elaboration of the analytical modelling method.

References

[1] Zhang Z, Wang X, Liu J, Dai C, Sun Y. Robotic micromanipulation: fundamentals and applications. Annu Rev Contr Robot Autonomous Syst 2019;2:181–203.

[2] Luu DK, Shi C, Sun Y. A review of nanomanipulation in scanning electron microscopes. Cham: Springer International Publishing; 2016. p. 347–79. https://doi.org/10.1007/978-3-319-23853-1_11.

[3] Lukkari MJ, Karjalainen MI, Sarkanen R, Linne ML, Jalonen TO, Kallio PJ. Electrical detection of the contact between a microinjection pipette and cells. In: Annual International Conference of the IEEE Engineering in Medicine and Biology - Proceedings. 26 IV; 2004. p. 2557–60.

[4] Gerena E, Legendre F, Vitry Y, Regnier S, Haliyo S. Improving optical micromanipulation with force-feedback bilateral coupling. IEEE Int Conf Robot Autom 2020:10292–8.

[5] Nafari A, Angenete J, Svensson K, Sanz-Velasco A, Enoksson P. MEMS sensor for in situ TEMnanoindentation with simultaneous force and current measurements. J Micromech Microeng 2010;20.

[6] Pillarisetti A, Pekarev M, Brooks AD, Desai JP. Evaluating the effect of force feedback in cell injection. IEEE Trans Autom Sci Eng 2007;4:322–31.

[7] Xu Q. Micromachines for biological micromanipulation. Micromachines for Biological Micromanipulation; 2018. p. 1–226.

[8] Liu X, Kim K, Zhang Y, Sun Y. Nanonewton force sensing and control in microrobotic cell manipulation. Int J Robot Res 2009;28:1065–76.

[9] Mekid S, Bashmal S, Ouakad HM. Nanoscale manipulators: review of conceptual designs through recent patents. Recent Patents Nanotechnol 2016;10:44–58.

[10] Mekid S, Bashmal S. Engineering manipulation at nanoscale: further functional specifications. J Eng Des Technol 2019;17:572–90.

[11] Lu W, Lieber CM. Nanoelectronics from the bottom up. Nanosci Technol 2009: 137–46.

[12] Chuancheng J, Lin Z, Huang Y, Duan X. Nanowire electronics: from nanoscale to macroscale. Chem Rev 2019;119.

[13] Gazibegovic S, Car D, Zhang H, Balk SC, Logan JA, De Moor MW, Cassidy MC, Schmits R, Xu D, Wang G, Krogstrup P, Op Het Veld RL, Zuo K, Vos Y, Shen J, Bouman D, Shojaei B, Pennachio D, Lee JS, Van Veldhoven PJ, Koelling S, Verheijen MA, Kouwenhoven LP, Palmstrøm CJ, Bakkers EP. Epitaxy of advanced nanowire quantum devices. Nature 2017;548:434–8.

[14] Jiang X, Tian B, Xiang J, Qian F, Zheng G, Wang H, Mai L, Lieber C. Rational growth of branched nanowire heterostructures with synthetically encoded properties and function. Proc Natl Acad Sci USA 2011;108:12212–6.

[15] Fang X-Q, Liu J-X, Gupta V. Fundamental formulations and recent achievements in piezoelectric nano-structures: a review. Nanoscale 2013;5:1716–26.

[16] Žukauskaitė A, Broitman E, Sandström P, Hultman L, Birch J. Nanoprobe mechanical and piezoelectric characterization of scxal1-xn(0001) thin films. Phys Status Solidi 2015;212:666–73.

[17] Ru C, Zhang Y, Sun Y, Zhong Y, Sun X, Hoyle D, Cotton I. Automated four-point probe measurement of nanowires inside a scanning electron microscope. IEEE Trans Nanotechnol 2011;10:674–81.

[18] Lee H, Cooper R, Wang K, Liang H. Nano-scale characterization of a piezoelectric polymer (polyvinylidene difluoride, pvdf). Sensors 2008;8:7359–68.

[19] Qu J, Liu X. Investigating the impact of SEM chamber conditions and imaging parameters on contact resistance of in situ nanoprobing. Nanotechnology 2017;28.

[20] Holm R. Electrical contacts - theory and application. fourth ed. 1967.

[21] Slade PG. Electrical contacts principles and applications. second ed. 2014.

[22] Park M, Cola BA, Siegmund T, Xu J, Maschmann MR, Fisher TS, Kim H. Effects of a carbon nanotube layer on electrical contact resistance between copper substrates. Nanotechnology 2006;17:2294–303.

[23] Lee Changyeol, Kim Yoonhyuk, Choi Yong-Gie, Cho Young-Ho, Lee Kwyro, Kwak Byung Man. High-density silicon microprobe arrays for lcd pixel inspection. In: Proceedings of ninth international workshop on micro electromechanical systems; 1996. p. 429–34. https://doi.org/10.1109/MEMSYS.1996.494020.

[24] Wei Y, Xu Q. An overview of micro-force sensing techniques. Sens Actuators, A 2015;234:359–74.

[25] Liang Q, Zhang D, Coppola G, Wang Y, Wei S, Ge Y. Multi-dimensional MEMS/micro sensor for force and moment sensing: a review. IEEE Sensor J 2014;14: 2643–57.

[26] Liu J, Draghi L, Bain JA, Schlesinger TE, Fedder GK. Three-dof CMOS-MEMS probes with embedded piezoresistive sensors. Proc - IEEE Int Conf Micro Electro Mech Syst (MEMS) 2010:284–7.

[27] Muntwyler S, Beyeler F, Nelson BJ. Three-axis micro-force sensor with sub-micro-Newton measurement uncertainty and tunable force range. J Micromech Microeng 2010;20.

[28] Cosandier F, Henein S, Richard M, Rubbert L. The art of flexure mechanism design. Lausanne: EPFL Press; 2017.

[29] Mishra MK, Dubey V, Mishra PM, Khan I. MEMS technology: a review. J Eng Res Rep 2019;4:1–24.

[30] Beinik I, Kratzer M, Wachauer A, Wang L, Lechner RT, Teichert C, Motz C, Anwand W, Brauer G, Chen XY, Hsu XY, Djurišić AB. Electrical properties of zno nanorods studied by conductive atomic force microscopy. J Appl Phys 2011;110: 052005.

[31] Shen Y, Winder E, Xi N, Pomeroy CA, Wejinya UC. Closed-loop optimal control-enabled piezoelectric microforce sensors. IEEE ASME Trans Mechatron 2006;11: 420–7.

[32] Liseli JB, Agnus J, Lutz P, Rakotondrabe M. An overview of piezoelectric self-sensing actuation for nanopositioning applications: electrical circuits, displacement, and force estimation. IEEE Trans Instrum Meas 2020;69:2–14.

[33] Masson L, Civet Y, Germano P, Perriard Y. Design of a generalised charge-based self-sensing model for quasi-static piezoelectric actuators. In: 2017 20th international conference on electrical machines and systems, ICEMS 2017; 2017. p. 8–13.

[34] Smreczak M, Baur C, Rubbert L. Design of a compliant load cell with adjustable stiffness. Precision Engineering; 2020.

[35] Glanville K, Petrie SF. Weights and balances in ancient Egypt. Nature 1936;137: 890–2.

[36] French MJ, Widden MB. The spring-and-lever balancing mechanism, George Carwardine and the Anglepoise lamp. Proc IME C J Mech Eng Sci 2000;214:501–7.

[37] Kahrobaiyan MH, Thalmann E, Rubbert L, Vardi I, Henein S. Gravity-insensitive flexure pivot oscillators. J Mech Des Trans ASME 2018;140:1–9.

[38] Marangoni RR, Rahneberg I, Hilbrunner F, Theska R, Fröhlich T. Analysis of weighing cells based on the principle of electromagnetic force compensation. Meas Sci Technol 2017;28.

[39] Arakelian V. Gravity compensation in robotics. Adv Robot 2016;30:79–96.

[40] Lu Q, Ortega C, Ma O. Passive gravity compensation mechanisms: technologies and applications. Recent Pat Eng 2011;5:32–44.

[41] Chheta Y, Joshi R, Gotewal KK, Manoahstephen M. A review on passive gravity compensation. In: Proceedings of the international conference on electronics, communication and aerospace technology, ICECA 2017 2017-janua; 2017. p. 184–9.

[42] Metzger A, Baltisberger S, Burkhard HR. Force-measuring device with sliding weight. Patent EP 2690415B1; 2012.

[43] Hauck T. Weighing sensor with a serial arrangement of force transfer levers to obtain a compact load cell. Patent US 8232484B2; 2011.

[44] Canevari LT. Series twin leaf spring weighing scale. Patent US 4022288A; 1977.

[45] Dunning A, Tolou N, Herder J. A compact low-stiffness six degrees of freedom compliant precision stage. Precis Eng 2013;37:380–8.

[46] Metzger A, Baltisberger S, Burkhard HR, Béguin C, Uster M. Weighing cell based on the principle of electromagnetic force compensation with optoelectronic position sensor. Patent US 9086315B2; 2015.

[47] Li X, Chung VPJ, Guney MG, Mukherjee T, Fedder GK, Paramesh J. A high dynamic range cmos-mems accelerometer array with drift compensation and fine-grain offset compensation. In: 2019 IEEE custom integrated circuits conference (CICC); 2019. p. 1–4.

[48] Maroufi M, Alemansour H, Bulut Coskun M, Reza Moheimani SO. An adjustable-stiffness MEMS force sensor: design, characterization, and control. Mechatronics 2018;56:198–210.

[49] Abadie J, Piat E, Oster S, Boukallel M. Modeling and experimentation of a passive low frequency nanoforce sensor based on diamagnetic levitation. Sens Actuators, A 2012;173:227–37.

[50] Radaelli G, Gallego JA, Herder JL. An energy approach to static balancing of systems with torsion stiffness. J Mech Des 2011;133:091006.

[51] Tissot-Daguette L, Henein S, Smreczak M, Dagon B. Flexure pivot based system. Holder: EPFL; 2020. Patent EP 20213347.6 - 1001.

[52] Tissot-Daguette L, Smreczak M, Baur C, Henein S. Load cell with adjustable stiffness based on a preloaded t-shaped flexure pivot. Euspen 2020:2021.

[53] Thalmann E. Flexure pivot oscillators for mechanical watches. Ph.D. thesis, École Polytechnique Fédérale de Lausanne; 2020.

[54] Hongzhe Z, Shusheng B. Accuracy characteristics of the generalized cross-spring pivot. Mech Mach Theor 2010;45:1434–48.

[55] Thalmann E, Kahrobaiyan MH, Vardi I, Henein S. Flexure pivot oscillator with intrinsically tuned isochronism. J Mech Des Trans ASME 2020;142:1–13.

[56] Wittrick WH. The properties of crossed flexure pivots, and the influence of the point at which the strips cross. Aeronaut Q 1951;2:272–92.

[57] Shusheng B, Hongzhe Z, Jingjun Y. Modeling of a cartwheel flexural pivot. J Mech Des Trans ASME 2009;131. 0610101–0610109.

[58] Bellouard Y. On the bending strength of fused silica flexures fabricated by ultrafast lasers. Opt Mater Express 2011;1:816–31.

[59] Franssila S, Tuomikoski S. Chapter 15 - mems lithography. In: Tilli M, Paulasto-Krockel M, Petzold M, Theuss H, Motooka T, Lindroos V, editors. Handbook of silicon based MEMS materials and technologies. third ed. Elsevier; 2020. p. 399–416. Micro and Nano Technologies, third edition ed. https://www.sciencedirect.com/science/article/pii/B9780128177860000153. https://doi.org/10.1016/B978-0-12-817786-0.00015-3.

[60] Guillaume C. Invar and elinvar. nobel lecture; 1920.

Michal Smreczak is currently a PhD student in Instant-Lab at École Polytechnique Fédérale de Lausanne (EPFL). He obtained his master's degree in Robotics at Wroclaw University of Science and Technology, Poland, in 2017. His academical research is oriented towards microrobotics, compliant mechanisms and force sensing technologies.

Loïc Tissot-Daguette works as a research assistant in the Micromechanical and Horological Design Laboratory (Instant-Lab), at Swiss Federal Institute of Technology (EPFL). He previously received the M.Sc. degree in micro-engineering with a specialization in robotics, from EPFL, in 2019. He is currently developing novel compliant mechanisms with nonlinear behaviors, such as constant-force, stiffness-tuning and bistable mechanisms

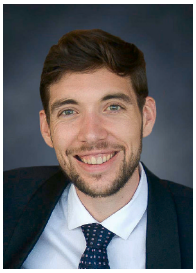

Etienne Thalmann is a postdoctoral researcher at EPFL's Micromechanical and Horological Design Laboratory (Instant-Lab). His research focuses on the design of compliant mechanisms. He completed his PhD in the same laboratory in 2020, on the topic of flexure pivot oscillators for mechanical watches. Previously, he received the MSc degree in Mechanical Engineering from EPFL in 2015 and conducted his Master's thesis in control systems at the Swiss Center for Electronics and Microtechnology (CSEM).

Charles Baur works as a senior scientist in Instant-Lab at École polytechnique fédérale de Lausanne (EPFL). He obtained his PhD degree in Microtechnology at EPFL in 1992. He has a wide experience in projects related to compliant structures and medtech.

Simon Henein - He obtained an engineering degree at the Ecole Polytechnique Fédérale de Lausanne (EPFL) in 1996 and went on to complete his doctorate at the EPFL in 2000. In 2001, he published the book "Conception des guidages flexibles" which has become a reference in precision engineering. Since November 1st, 2012, he is associate professor in micro-engineering at the EPFL, holder of the Patek Philippe Chair and director of the Micromechanical and horological design laboratory (Instant-Lab).